

國立臺灣大學工學院化學工程學研究所

碩士論文

Department of Chemical Engineering

College of Engineering

National Taiwan University

Master Thesis



奈米孔道的電動力學行為：

不連續截面與介電性質的影響

Electrokinetic Behaviors of Nanochannels: Influences of
Nonuniform Cross Section and Dielectric Properties

嚴維寬

Wei-Kuan Yen

指導教授：徐治平 博士

Advisor: Jyh-Ping Hsu, Ph.D.

中華民國 109 年 6 月

June, 2020

致謝

下筆之時，腦中瞬時浮現的畫面是甫升大一時的青澀模樣以及其他片段化的零小回憶，於此的我不禁面露微笑且深感滿足；而後腦海中出現的是這六年來一路上給予我幫助、溫暖的人事物，此刻，先前的笑容黯然消逝，因為我知道自己是何其幸運才能從其他人身上收穫，必須詳以銘記。

首先想感謝治平老師給予研究上的自主安排，其中特別感謝老師能支持我更動論文題目的意願，對於當日在辦公室談論此事時，老師給予的勉勵印象猶新，實為感動。另外也感謝老師讓我代表參與您的終生成就頒獎儀式，這個活動對我的人生亦意義非凡，在活動中我看到與會嘉賓們對於自己付諸努力的領域是如何的有熱情與自信，那樣的情景給我許多感動，也讓我重新燃起追逐自己心中想找尋的熱情，利用研究之餘的時間，我也不馬虎的持續找尋屬於自己的成就。

感謝志原學長在提供研究協助之餘，還帶著我在球場上來回奔馳，揮灑汗水；感謝采葳、子喬、永哲作為實驗室的榜樣帶領我們，亦是生活上的好朋友；感謝政楷、昱廷、嘉陽帶來的歡樂，期待你們接下來能持續增長，滋養後輩！

特別感謝偉誠在大學、研究所的相伴，不諱言地說真的在課業上受到了你很多的照顧，因此也讓我自已有許多時間進行其他方面的涉略；在生活層面你真的是一個最棒的朋友，那種以朋友為最高順位的態度在台大這樣的環境真的相對罕見，是我少數看過最符合「完人」的人。俊廷，感謝你分享許多特別的人生歷程，也很佩服你可以在逆境中成長，甚至可以維持心態；另外也從你身上學到不只把一件事情完成，更要把它做到好的態度，這點非常觸動到我。宗諺，還記得大學實驗課分到同一組，當時就看的出來你對研究的熱情，碩士班期間你閱覽論文的態度更是蕪露無遺，非常看好你博士班的表現！佳蓉，相處的記憶幾乎凍結在碩一的期間，感謝妳晚上聆聽我生活的苦悶，還有懷念以前妳打電動時凶狠的反差感，哈！

感謝女友幸愉，讓我重視工作與生活間應有的平衡，在研究所的期間也共度許多有趣的、深植腦海的體驗，期待未來的日子能持續有所收穫。感謝家人，雖然這兩年的期間較少有機會相聚，但來自聲音、文字的鼓勵依然給予我很大的支持作用。

六年的台大旅程，正式謝幕，或非絕倫，但仍精彩。

維寬 2020.7 誌於國立台灣大學 化學工程學系

國立臺灣大學碩士學位論文
口試委員會審定書

奈米孔道的電動力學行為：

不連續截面與介電性質的影響

Electrokinetic Behaviors of Nanochannels: Influences of
Nonuniform Cross Section and Dielectric Properties

本論文係嚴維寬君（學號 R07524066）在國立臺灣大學化學工程
學系、所完成之碩士學位論文，於民國一〇九年六月二十三日承下列
考試委員審查通過及口試及格，特此證明

口試委員：

3111) (簽名)

(指導教授)
曾瑞琪 張有義

林志原

林祥泰 (簽名)

系主任、所長

(是否須簽章依各院系所規定)

中文摘要

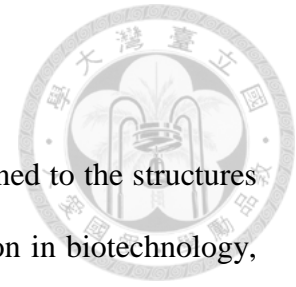
奈米流體為一門專門探討流體侷限於奈米尺度結構的學問。近年來由於其在生醫領域的應用，已有許多針對諸如離子整流效應及離子選擇性等離子傳輸現象的研究發表於世。

第一章節中，我們針對一串聯不同截面大小之圓形直管，且可受 pH 調控的奈米孔道進行探討，並專注於探討兩直管半徑、長度的比例，以及濃度和溶液酸鹼值所造成的影響。數值模擬的結果顯示，整流效應係數會隨著半徑、長度比例的變化而呈現局部最大值，並且該值隨著濃度的變化出現在不同的尺度比例上。除此之外，溶液酸鹼值對於整流效應係數的影響亦出現局部最大值；從通篇的結果可以觀察到溶液酸鹼值對於此奈米孔道的整流行為有最顯著的影響。以上研究成果已發表於國際期刊 *Electrophoresis*。

第二章節中，我們以數值模擬探討介電薄膜對於帶電表面和離子之間的靜電作用力的影響；其中與過去相關研究不同的地方是，本研究採用基於 Poisson–Nernst–Planck 以及 Navier–Stokes 方程式的連續方程式，並運用其計算離子電導值。在本章節研究中，主要探討薄膜自體的介電係數對於圓管狀奈米孔道的離子傳輸行為的影響，並輔以探討奈米孔道的尺寸、溶液的濃度以及酸鹼度對其造成的影響。

關鍵字: 離子整流；不連續截面；表面極化；介電效應

Abstract



Nanofluidic is the study of the transport of fluids that are confined to the structures of the nanometer length scale. In recent years, due to the application in biotechnology, several interests such as ion current rectification (ICR) and ionic selectivity have been investigated.

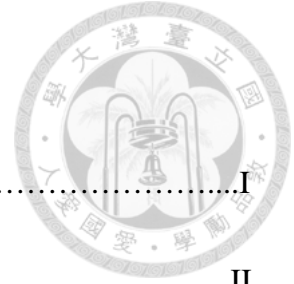
In chapter 1, the ICR behavior of a pH-regulated nanochannel comprising two series connected cylindrical nanochannels of different radii is examined theoretically, focusing on the influences of the radii ratio, the length ratio, the bulk concentration, and the solution pH. The results of numerical simulation reveal that the rectification factor exhibits a local maximum with respect to both the radii ratio and the length ratio. The values of the radii ratio and the length ratio at which the local maximum in the rectification factor occur depend upon the level of the bulk salt concentration. The rectification factor also shows a local maximum as the solution pH varies. Among the factors examined, the solution pH influences the ICR behavior of the nanochannel most significantly. The above results were published in *Electrophoresis*.

In chapter 2, we demonstrate a theoretical model to investigate how a dielectric membrane governs the electrostatic interaction between ions and charged surfaces via the induced dipole. The model is based on the continuum dynamics composed of the Poisson–Nernst–Planck and the Navier–Stokes equations to calculate the ionic conductance. In this study, we focus on the influence of the permittivity of the membrane on a cylindrical nanopore, in addition, we explore the effects of dimension of nanopores, electrolyte concentration, and electrolyte pH.

Keywords: ionic current rectification, nonuniform cross section, surface polarization, dielectric effect.



Contents



中文摘要.....	I
Abstract	II
Contents.....	IV
List of Tables.....	V
List of Figures.....	VI
Chapter 1 Ion Current Rectification Behavior of a Nanochannel Having Nonuniform Cross Section	1
References of Chapter 1	17
Chapter 2 Eletrokinetic Behavior of a pH-regulated, Dielectric Cylindrical Nanopore	36
References of Chapter 2	53
Conclusion	68

List of Tables

Table 2-1. Boundary conditions assumed for eq (1)-(6)..... 57



List of Figures

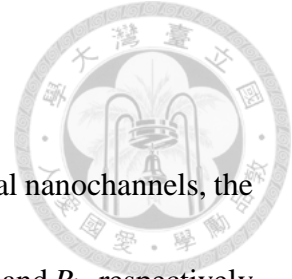


Figure 1-1. A nanochannel comprises two series connected cylindrical nanochannels, the length and the radius of the base end section of the nanochannel are L_b and R_b , respectively, and L_t and R_t are the length and the radius of the tip end section of the nanochannel.... 23

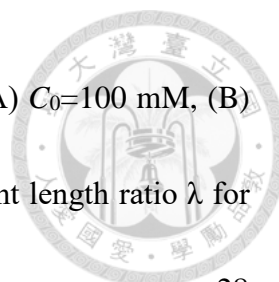
Figure 1-2. Simulated $I-V_{app}$ curves for various combinations of the bulk salt concentration C_0 and the segment radii ratio γ at pH 4 and $\lambda=0.5$. (A) $C_0=100$ mM, (B) $C_0=10$ mM, (C) $C_0=1$ mM, (D) $C_0=0.1$ mM KCl..... 24

Figure 1-3. (A) Variation of R_f with the bulk salt concentration C_0 for various values of γ . (B) Variation of R_f with the segment radii ratio γ for various levels of the bulk salt concentration C_0 . pH is 4 and $\lambda=0.5$ in both cases..... 25

Figure 1-4. Axial variation in the cross-sectional averaged ionic conductivity for various values of γ at pH 4 and $\lambda=0.5$. (A) $C_0=100$ mM, (B) $C_0=10$ mM, (C) $C_0=1$ mM, (D) $C_0=0.1$ mM KCl. Solid curves: $V_{app}=-1$ V; dash curves: $V_{app}=+1$ V..... 26

Figure 1-5. Axial variation in the cross-sectional averaged electric potential for various values of γ at pH 4 and $\lambda=0.5$. (A) $C_0=100$ mM, (B) $C_0=10$ mM, (C) $C_0=1$ mM, (D) $C_0=0.1$ mM. Solid curves: $V_{app}=-1$ V; dash curves: $V_{app}=+1$ V. Shaded areas denote the nanochannel interior..... 27

Figure 1-6. Simulated $I-V_{app}$ curves for various combinations of the bulk salt



concentration C_0 and the segment length ratio λ at pH 4 and $\gamma=3$. (A) $C_0=100$ mM, (B) $C_0=10$ mM, (C) $C_0=1$ mM KCl. (D) Variation of R_f with the segment length ratio λ for various levels of the bulk salt concentration C_0 28

Figure 1-7. Axial variation in the cross-sectional averaged ionic conductivity for various values of λ at pH 4 and $\gamma=3$. (A) $C_0=100$ mM, (B) $C_0=10$ mM, (C) $C_0=1$ mM KCl. Solid curves: $V_{app}=-1$ V; dashed curves: $V_{app}=+1$ V..... 29

Figure 1-8. (A) Variation of the ICR factor R_f with pH. (B) Axial variation in the cross-sectional averaged ionic conductivity for various values of pH. Solid curves: $V_{app}=+1$ V; dashed curves: $V_{app}=-1$ V. (C) Variation of $|I|$ with pH at $V_{app}=\pm 1$ V. Parameters assumed are $\lambda=0.15$ and $\gamma=3$ and $C_0=1$ mM KCl. 30

Figure 1-S1. Variation of the ionic current I with the segment radii ratio γ at various levels of the bulk salt concentration C_0 at $\lambda=0.5$. (A) $V_{app}=+1$ V, (B) $V_{app}=-1$ V. 31

Figure 1-S2. Simulated $I-V_{app}$ curves for various combinations of the bulk salt concentration C_0 at pH 4 and $\gamma=3$. (A) $C_0=100$ mM, (B) $C_0=10$ mM, (C) $C_0=1$ mM, (D) $C_0=0.1$ mM KCl. The contributions of the migration and the diffusion terms in eq (3) to I are also presented. 32

Figure 1-S3. Simulated $I-V_{app}$ curves for various combinations of ion species at pH 4, $\gamma=3$ and $\lambda=0.5$. (A) $C_0=1$ mM, (B) $C_0=100$ mM. 33



Figure 1-S4. Axial variation in the cross-sectional averaged concentration for both cations and anions at pH 4, $\gamma=3$ and $\lambda=0.5$. (A) $C_0=1$ mM, (B) $C_0=100$ mM KCl. Solid curves: $V_{app}=-1$ V; dashed curves: $V_{app}=+1$ V..... 34

Figure 1-S5. Variation of R_f with the segment length ratio λ for various levels of L_{total} at pH 4, $\gamma=3$ and $C_0=100$ mM KCl..... 35

Figure 2-1. A charged cylindrical nanochannel of radius R_n and axial length L_n prepared from a dielectric membrane. The nanochannel connects two large, identical reservoirs filled with an aqueous salt solution. A computation domain Ω comprising the nanochannel and a cylindrical domain of length L_r and R_r in each reservoir is defined. The upper reservoir is grounded, and a potential bias V_0 is applied to the lower one. The cylindrical coordinates (r, z) are adopted with the origin at the nanochannel center. 58

Figure 2-2. (a) Variation of nanopore conductance G with its length L_n at various levels of ϵm , (a), and variation with ϵm at various levels of L_n , (b), at $Cb = 3$ mM, $R_n=5$ nm, and pH 4. Insert in (a): variation of the conductance ratio $n = G(\epsilon m = 80)/G(\epsilon m = 0)$ against L_n 59

Figure 2-3. Cross-sectional averaged concentration profile of K^+ and Cl^- at pH 4 and $Cb = 3$ mM, and the radius of nanopore $R_n=5$ nm. (a) $L_n=20$ nm, (b) $L_n=50$ nm, (c) $L_n=100$ nm, (d) $L_n=1000$ nm..... 60

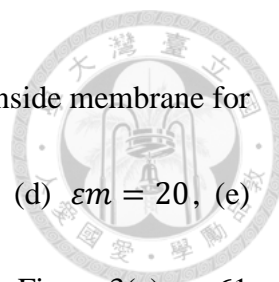


Figure 2-4. Profiles of the electric potential in the liquid phase and inside membrane for various levels of ϵm . (a) $\epsilon m = 0$, (b) $\epsilon m = 0.1$, (c) $\epsilon m = 10$, (d) $\epsilon m = 20$, (e) $\epsilon m = 40$, (f) $\epsilon m = 80$. The parameters used are the same as those in Figure 3(a)..... 61

Figure 2-5. (a) Conductance of the nanopore versus the pH for $\epsilon m = 80$ and 0 at $C_b = 3$ mM and the dimensions of nanopore $L_n = 20$ nm, $R_n = 5$ nm. (b) Cross-sectional averaged concentration profile of K^+ and Cl^- at pH 7..... 62

Figure 2-6. (a) Conductance of the nanopore versus C_b for $\epsilon m = 80$ and 0 at pH 4 and the dimensions of nanopore $L_n = 20$ nm, $R_n = 5$ nm. (b) Cross-sectional averaged concentration profile of K^+ and Cl^- at $C_b = 500$ mM..... 63

Figure 2-S1. Conductance in a pH-regulated silica nanopore of length $L_n=34$ nm as a function of C_b at pH 7.5: symbols with error bars are selected from the experimental data of Smeets et al.; solid lines present the numerical results at $R_n=5.1$ nm, $pK_A=7$, $pK_b=1.9$, $\Gamma t=4.8$ nm² and $\epsilon m=3.8$ [R]..... 64

Figure 2-S2. Simulated current-voltage curves for various levels of ϵm at $R_n=5$ nm, $L_n=20$ nm, $C_b = 3$ mM, and pH 4..... 65

Figure 2-S3. Axial variations in the cross-sectional averaged electric potentials φ and Ψ for various values of L_n at $C_b = 3$ mM, $R_n=5$ nm, and pH 4. (a) $L_n=20$ nm, (b) $L_n=50$ nm, (c) $L_n=100$ nm, (d) $L_n=1000$ nm..... 66



Chapter 1



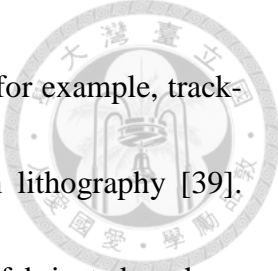
Ion Current Rectification Behavior of a Nanochannel Having Nonuniform Cross Section

Reproduced with permission from *Electrophoresis* 41 (2020) 802-810
Copyright 2020 Wiley

1-1. Introduction


Solid-state nanochannels/nanopores are adopted widely to simulate the ionic transport in biological systems, and various applications proposed, recently. The latter includes, for example, ionic gates [1, 2], nanofluidic diodes [3-6], energy conversion [7, 8], and filtration/desalination [9, 10]. The phenomena and mechanisms associated to nanochannels/nanopores rest mainly on the nonuniform distribution of ion species and the overlapping of the electric double layer (EDL) in their interior [11, 12]. The overlapping of EDL influences significantly the transport of ions inside a nanochannel/nanopore, yielding interesting and important phenomena such as ion concentration polarization (ICP) [13, 14], ion selectivity [15, 16], and ionic current rectification (ICR) [17-19].

ICR, an asymmetric current-voltage behavior when the potential polarity is switched, has been identified in several logic nanofluidic devices [1-6]. Through many experimental and theoretical studies conducted in the last decades, it has been concluded that the ICR phenomenon of nanochannels/nanopores can be attributed to their asymmetric characteristics. These include, for instance, geometry [20-28], surface charge [29, 30], chemical composition [31, 32], wettability [33], and external applied fields such as pH gradient [34], electrolyte concentration gradient [35], and pressure gradient [36]. Among these, geometry-induced ICR draws much attention because the associated nanochannel



fabrication methods are convenient and controllable. These include, for example, track-etching [37], focused ion beam sculpting [38], and electron-beam lithography [39]. Through these methods, various types of nanochannel have been fabricated such as cylindrical [27], conical [22], hourglass-shaped [26], cigar-shaped [20], bullet-shaped [25], dumbbell-shaped [21], and funnel-shaped [23]. The ICR behavior of an asymmetric nanochannel can be influenced by factors including ionic species [40], ion concentration [35, 41], applied electric potential [40], pH [42, 43], temperature [44], and nanochannel length and its opening radii [24, 45, 46]. The cone angle [24] and the ratio of (cylindrical segment/conical segment) [23] are important to conical and funnel-shaped nanochannels, respectively.

Previous studies regarding asymmetric nanochannel focused mainly on polymeric material such as polycarbonate (PC) [47], polyethylene terephthalate (PET) [46], and polyimide (PI) [48] nanochannel. Due to the low porosity of polymer material, the nanochannels made of its membrane are not suitable for large scale applications. In contrast, inorganic membrane such as anodic aluminum oxide (AAO) membrane can have ordered pores with a high pore density is more satisfactory and desirable. However, inorganic nanochannels are usually cylindrical, and therefore, exhibiting no ICR phenomenon due their symmetric structure. This disadvantage can be circumvented by a

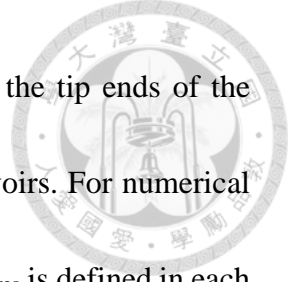


series connection of two cylindrical nanochannels of different radii, yielding a longer nanochannel having a nonuniform cross section [49]. The branched nanochannel adopted by Kong et al. [42] and Li et al. [43] is another type of asymmetric AAO nanochannel having a nonuniform cross section.

Note that for a fixed axial length, the cone angle of a conical nanochannel is equivalent to the ratio of (base radius/tip radius), and for a funnel-shaped nanochannel, the length ratio of (cylindrical section/conical section) is analogous to that of a nanochannel comprising two cylindrical sections of different radii. Considering an AAO nanochannel, we analyze theoretically the influence of the geometry of a nanochannel on its ICR behavior in this study. Taking account of the effects of electroosmosis and the pH-regulated nature of the nanochannel surface, a thorough numerical simulation is conducted by considering factors including the solution pH, the ion concentration, the radii ratio, and the segment lengths ratio.

1-2. Theoretical Model

As shown in Figure 1-1, the system under consideration comprises two series connected cylindrical nanochannels. The length and the radius of the base end section of the nanochannel are L_b and R_b , respectively, and L_t and R_t are the length and the radius of



the tip end section of the nanochannel, respectively. The base and the tip ends of the nanochannel are connected to two identical, large, cylindrical reservoirs. For numerical simulation purpose, a computation domain of length L_{res} and radius R_{res} is defined in each reservoir. A voltage bias V_{app} is applied across the nanochannel with its tip end side grounded. The system is filled with an aqueous, monovalent salt solution of bulk molar concentration C_b . The cylindrical coordinates (r, θ, z) are adopted with the origin at the center of the connection of the two sub-nanochannels.

The nanochannel is made of an amphoteric metal oxide material having functional groups $M-OH$ capable of undergoing reactions $M-OH+H^+\rightleftharpoons M-OH_2^+$ and $M-OH\rightleftharpoons M-O^-+H^+$ with equilibrium constant K_B and K_A , respectively. If we let e be the elementary charge, N_{site} the density of the surface functional groups, and $[H^+]_s$ the surface concentration of H^+ , then the charge density of the nanochannel surface σ_s is [50, 51]

$$\sigma_s = -10^{18} e N_{site} \left\{ \frac{10^{-pK_A} - 10^{-pK_B} ([H^+]_s)^2}{10^{-pK_A} + 10^{-pK_B} ([H^+]_s)^2 + [H^+]_s} \right\} \quad (1)$$

where $pK_B = -\log K_B$, and $pK_A = -\log K_A$

The present problem is described by the following Poisson-Nernst-Planck (PNP) and modified Navier-Stokes (NS) equations [52]:

$$-\varepsilon_f \nabla^2 \phi = \sum_{i=1}^4 F Z_i c_i \quad (2)$$

$$\nabla \cdot \mathbf{J}_i = \nabla \cdot \left[\mathbf{u} c_i - D_i \nabla c_i - \frac{z_i F}{RT} D_i c_i \nabla \phi \right] = 0 \quad (3)$$



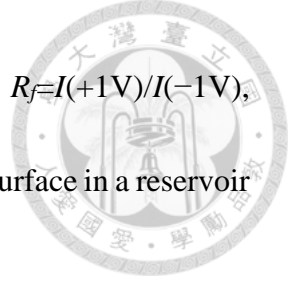
$$-\nabla p + \mu \nabla^2 \mathbf{u} - \sum_{i=1}^4 F z_i c_i \nabla \phi = 0 \quad (4)$$

$$\nabla \cdot \mathbf{u} = 0 \quad (5)$$

ε_f , μ , R , F , T , and M are the fluid permittivity, its fluid viscosity, gas constant, Faraday constant, the absolute temperature, and the types of ionic species, respectively. ϕ , \mathbf{u} , and p are the electric potential, the fluid velocity, and the hydrodynamic pressure, respectively. \mathbf{J}_i , D_i , c_i , and z_i are the ionic flux, diffusivity, molar concentration, and valence of the i^{th} ionic species, respectively.

Referring to Figure 1-1, to specify the boundary conditions associated with Eqs. (2)-(5) we assume the following. (i) The salt concentration on both ends of the computation domain (blue boundary) reaches the bulk value. (ii) No external pressure gradient is applied to the system. (iii) The rigid wall of the nanochannel (red boundary) has the charge density σ_s , and is no-slip ($\mathbf{u}=\mathbf{0}$) and ion-impenetrable ($\mathbf{n} \cdot \mathbf{J}_i=0$), with \mathbf{n} being the unit outer normal vector. (iv) The boundaries of the computation domain (black boundaries) are slip.

The present problem is solved numerically by COMSOL Multiphysics (version 5.4). Mesh independence is checked throughout the solution procedure, and code verification conducted to ensure its applicability. Typically, with a finer mesh employed near the nanochannel surface, using ca. 200,000 meshes is enough for obtaining reliable and



accurate results. For convenience, we defined the ICR factor R_f as $R_f = I(+1V)/I(-1V)$, where the ionic current is $I = \int_A \mathbf{F}(\sum_{i=1}^4 z_i \mathbf{J}_i) \cdot \mathbf{n} dA$, with A being the surface in a reservoir perpendicular to the nanochannel axis.

1-3. Results and Discussion

We assume the following: $L_{\text{total}} = L_t + L_b = 2 \mu\text{m}$, $R_{\text{res}} = 3 \mu\text{m}$, $L_{\text{res}} = 3 \mu\text{m}$, $R_t = 30 \text{ nm}$, $R = 8.314 \text{ JK}^{-1}\text{mol}^{-1}$, $F = 96500 \text{ Cmol}^{-1}$, $T = 298\text{K}$, and $\mu = 0.001 \text{ Pa}\cdot\text{s}$. For convenience, we define $\lambda = L_t/L_{\text{total}}$ and $\gamma = R_b/R_t$. The nanochannel material is anodic aluminum oxide (AAO) with $N_{\text{site}} = 1 \text{ site/nm}^2$, $\text{pK}_A = 10$, and $\text{pK}_B = -6$ so that the isoelectric point (IEP) is 8 [50, 51]. The liquid phase is an aqueous KCl solution with its pH adjusted by HCl and KOH. This implies that four kinds of ionic species are present: H^+ , K^+ , Cl^- , and OH^- . If subscripts 1-4 denote H^+ , K^+ , Cl^- , and OH^- , respectively, then $D_1 = 9.31 \times 10^{-9} \text{ m}^2\text{s}^{-1}$, $D_2 = 1.96 \times 10^{-9} \text{ m}^2\text{s}^{-1}$, $D_3 = 2.03 \times 10^{-9} \text{ m}^2\text{s}^{-1}$, and $D_4 = 5.30 \times 10^{-9} \text{ m}^2\text{s}^{-1}$. Let C_{10} , C_{20} , C_{30} , and C_{40} (mM) be the bulk molar concentrations of those ions, respectively. Then $C_{10} = 10^{-\text{pH}+3}$, $C_{20} = C_b$, $C_{30} = C_b + 10^{-\text{pH}+3} - 10^{-(14-\text{pH})+3}$, and $C_{40} = 10^{-(14-\text{pH})+3}$ for $\text{pH} \leq 7$; $C_{10} = 10^{-\text{pH}+3}$, $C_{20} = C_b - 10^{-\text{pH}+3} + 10^{-(14-\text{pH})+3}$, $C_{30} = C_b$, and $C_{40} = 10^{-(14-\text{pH})+3}$ for $\text{pH} > 7$. The applied voltage bias V_{app} ranges from -1 to 1 V.

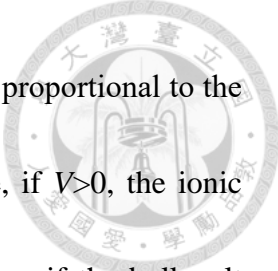


1-3-1. Influence of Parameter $\gamma=R_b/R_t$

The simulated $I-V_{app}$ curves for various combinations of the bulk salt concentration C_0 and the segment radii ratio γ at pH 4 shown in Figure 1-2 reveal that if the nanochannel is positively charged (pH<IEP), it exhibits an ICR behavior, where $I(V_{app}>0)$ is larger than corresponding $I(V_{app}<0)$.

As seen in Figure 1-3A, when the bulk salt concentration varies the ICR factor R_f shows a local maximum, which was reported previously [53]. Note that, as seen in Figure 1-3B, R_f also shows a local maximum as γ varies. To explain the ICR behaviors observed in Figures 1-2 and 1-3, we plot the axial variation in the cross-sectional averaged ionic conductivity $\Lambda=\int \sum_{i=1}^4 C_i \Lambda_i dA$ at $V_{app}=\pm 1$ V in Figure 1-4, and the axial variation in the cross-sectional averaged electric potential at $V_{app}=\pm 1$ V in Figure 1-5. Here, Λ_i is the limiting molar conductivity of ionic species i , and we assume that $\Lambda_1(H^+)$, $\Lambda_2(K^+)$, $\Lambda_3(Cl^-)$, and $\Lambda_4(OH^-)$ are 34.982, 7.352, 7.634, and 19.8 $mS \cdot m^2 \cdot mol^{-1}$ [54], respectively.

The profiles of the conductivity Λ shown in Figure 1-4 reveals that $\Lambda(V_{app} = +1$ V) is always larger than $\Lambda(V_{app} = -1$ V). This is because ion enrichment (depletion) occurs inside the nanochannel in the former (latter) so that $I(V_{app} = +1$ V) is larger than $I(V_{app} = -1$ V). As seen in Figure 1-4A, if the bulk salt concentration is sufficiently high (100 mM), $\Lambda(V_{app} = -1$ V) is insensitive to the variation in γ , implying that the ionic




flux is also insensitive to the variation in γ . Since the ionic current is proportional to the ionic flux, and inversely proportional to the nanochannel resistance, if $V > 0$, the ionic current increases with increasing γ , as seen in Figure 1-2A. However, if the bulk salt concentration is low, the EDL overlapping inside the nanochannel is significant, and it is sensitive to the nanochannel geometry so that the profile of Λ depends on the level of γ , and then the contribution of the nanochannel resistance to the ionic current become less significant. The behaviors of $I(V_{\text{app}} = +1 \text{ V})$ at various levels of C_0 (Figure 1-2A-C) are not surprising. Taking Figure 1-2B as an example, as γ increases although I is inversely proportional to the nanochannel resistance, $I(V_{\text{app}} = +1 \text{ V})$ does not increase monotonously with γ . This can be explained by noting that the profile of Λ shown in Figure 1-4B is consistent with that of the corresponding $I-V_{\text{app}}$ curve shown in Figure 1-2B. For the ranges of the parameters considered, the influence of ion enrichment on I at $V_{\text{app}} = +1 \text{ V}$ is much more significant than that of nanochannel resistance, and therefore, I exhibits a local maximum as γ varies (Figure 1-S1). Note that for the case of $V_{\text{app}} > 0$, if C_0 is lowered to 0.1 mM (Figure 1-2D), I approaches a plateau value as V_{app} gets large. Although the EDL overlapping is significant in this case, the direction of electromigration is opposite to that of ionic diffusion so that the contribution of the former to the net ionic flux is suppressed by that of the latter. In contrast, if C_0 is high, the direction of

electromigration is the same as that of ionic diffusion so that the contribution of the former to the ionic flux is enhanced by that of the latter, as seen in Figure 1-S2.

The contribution of each type of ion to the ionic current I at two levels of bulk salt concentration C_0 is illustrated in Figure 1-S3 for the case of pH 4, where the nanochannel is anion-selective. As seen in Figure 1-S3A, if C_0 is low (1 mM), the ionic current is contributed mainly by Cl^- , and the contributions of all the other types of ions are not significant. If C_0 is raised to 100 mM, the contributions of K^+ and Cl^- become appreciable, while those of H^+ and OH^- are still not significant.

The profiles of the electric potential ϕ shown in Figure 1-5 suggest that if the bulk salt concentration C_0 is low and $V_{\text{app}} > 0$ (Figure 1-5C-D), the distribution of ions is dominated by the charged nanochannel surface. In this case, a considerable amount of energy is consumed in driven the anions of the tip side reservoir into the nanochannel through applying V_{app} , yielding a rapid drop in ϕ . As illustrated in Figure 1-S4, if C_0 is low (1 mM), the concentration of anions near the nanochannel tip end is much higher than that in the reservoir. This leads to a high reverse diffusion potential, thereby reducing appreciably the applied electric potential. If C_0 is raised to 100 mM, that diffusion potential decreases appreciably so that the decrease in the applied electric potential becomes insignificant.



Similar to the case of $V_{app}>0$, if $V_{app}<0$, the ϕ near the junction of two nanochannel segments drops rapidly due to the driven of anions from the base side (lower conductivity) to the tip side (higher conductivity). In general, the larger the γ the higher the ϕ . In addition, the slope of each curve in Figure 1-5 is nearly constant in both the tip-end and the base-end segments of the nanochannel, but the slopes of the curves at the segment junction are different. This implies that for a fixed value of γ the electric field is nearly constant in each segment of the nanochannel, but the electric field in the tip-end segment is different from that in the base-end segment. In our case, the resistance is proportional to the slope of a curve in Figure 1-5, which shows that the difference in the resistance of the tip-end segment and that in the base-end segment increases with increasing γ , as mentioned previously. These explain the presence of a local maximum in R_f seen in Figure 1-3B.

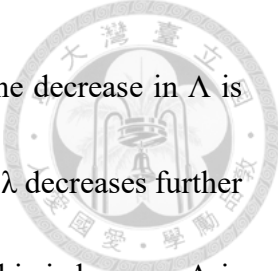
1-3-2. Influence of Parameter $\lambda=L_t/L_{total}$

As seen in Figure 1-6A-C, the higher the salt concentration C_0 the more appreciable the dependence of $|I|(V_{app}>0)$ on λ . Note that for all the levels of C_0 examined, $|I|$ does not vary monotonically with λ . As will be discussed later, this can be attributed to the competition between the conductivity and the nanochannel resistance. As can be seen in



Figure 1-6D, R_f has a local maximum occurring at a small value of λ (i.e., the degree of asymmetry of the nanochannel is large).

The results seen in Figure 1-6 can be explained further by the profile of the conductivity Λ illustrated in Figure 1-7. Figure 1-7A indicates that if $C_0=100$ mM and $V_{app}=+1$ V, Λ increases when λ is lowered from 0.8 to 0.15, but if λ is further lowered from 0.15 to 0.02, Λ decreases. However, due to the decrease in the nanochannel resistance, the corresponding current (Figure 1-6A) increases monotonically with decreasing λ in both intervals. In addition, in the first interval of λ , the influence of λ on Λ and that of nanochannel resistance on Λ are additive. This is not the case in the second interval, so that the rate of increase in Λ as λ decreases in the first interval is faster than that in the second interval. In contrast, if $V_{app}=-1$ V, Λ decreases with decreasing λ , in general, but $|I|$ increases with decreasing λ . This is because for $0.8>\lambda>0.15$, Λ decreases significantly with decreasing λ , offsetting the effect of the decrease in the nanochannel resistance so that $|I|$ decreases. In contrast, since Λ insensitive to the decrease in λ for $0.8>\lambda>0.15$, $|I|$ increases appreciably with decreasing λ due to the decrease in the nanochannel resistance. However, if C_0 is lowered to 1 mM, the decreases in λ from 0.8 to 0.15 at $V_{app}=-1$ V (Figure 1-7C), leads to a decrease in $|I|$ (Figure 1-6C). This is because the ion transport is dominated by the charged nanochannel surface in the present

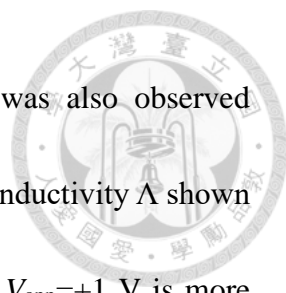


case, as mentioned in the previous section, so that the influence of the decrease in Λ is more important than that of the decrease in nanochannel resistance. If λ decreases further from 0.15 to 0.02, $|I|$ increases. As is in the case of $C_0=100$ mM, this is because Λ is insensitive to the decrease in λ for $0.15 > \lambda > 0.02$ so that $|I|$ is governed by the nanochannel resistance.

The influence of the nanochannel length L_{total} on the nanochannel performance is shown in Figure 1-S5 of the Supporting Information. In general, the longer the nanochannel the less satisfactory its ICR performance (i.e., smaller R_f). Note that the longer the nanochannel, the smaller the value of λ at which the local maximum of R_f occurs.

1-3-3. Influence of pH

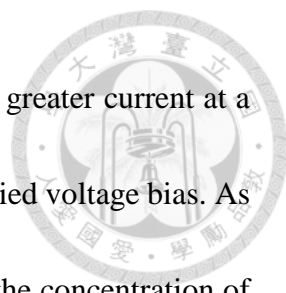
For convenience, we consider the case of $\text{pH} < \text{IEP}$ only, where the nanochannel surface is positively charged. The behaviors for the case of $\text{pH} > \text{IEP}$, where the nanochannel surface is negatively charged can be inferred from those for the case of $\text{pH} < \text{IEP}$. According to Eq (1), the more the pH deviates from IEP the higher the surface charge density. As seen in Figure 1-8A the nanochannel does not show ICR behavior at pH 8 (i.e., IEP), which is expected since the nanochannel surface is uncharged in this case.



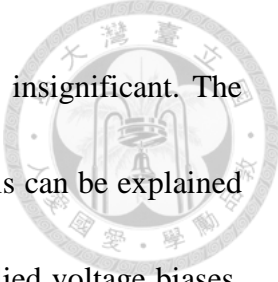
As pH decreases from 8, R_f exhibits a local maximum, which was also observed previously [55]. Again, this can be interpreted by the profile of the conductivity Λ shown in Figure 1-8B. As pH declines from 7.5 to 6, the increase in Λ at $V_{app}=+1$ V is more appreciable than that at $V_{app}=-1$ V. In this range of pH, the negative applied bias ($V_{app}=-1$ V) is sufficiently strong to drive out the counterions in the nanochannel, yielding a small Λ . As pH declines from 6 to 4, both $\Lambda(V_{app}=+1$ V) and $\Lambda(V_{app}=-1$ V) increase, implying that $V_{app}=-1$ V is unable to suppress the counterions in the nanochannel. In addition, the increase in $\Lambda(V_{app}=-1$ V) is larger than that in $\Lambda(V_{app}=+1$ V). To further understand the contributions of $\Lambda(V_{app}=+1$ V) and $\Lambda(V_{app}=-1$ V) shown in Figure 1-8B to ionic current, we plot $|I|$ against pH in Figure 1-8C. This figure reveals that if pH is close to IEP, $|I(V_{app} = -1 \text{ V})|$ is nearly constant, and the larger the deviation of pH from IEP the larger the $|I(V_{app} = -1 \text{ V})|$. This verifies the presence of the local maximum of R_f in Figure 1-8A.

1-4. Conclusions

The ionic current rectification (ICR) behavior of a nanochannel having a nonuniform cross-section is studied theoretically by considering a nanochannel comprising two series connected, pH-regulated cylindrical nanochannels of different radii. We show that a large



ratio γ (=radius of larger channel/radius of smaller channel) yields a greater current at a negatively applied voltage bias, but not necessary at a positively applied voltage bias. As γ increases the nanochannel resistance decreases monotonically but the concentration of ions in the nanochannel shows a local maximum, and the latter effect dominates the current. If a positive voltage bias is applied, the enrichment of ions in the nanochannel makes the interaction of ions and nanochannel surface important. In this case, the geometry of the nanochannel is important because it influences directly on the profile of ions inside. In contrast, if a negative voltage bias is applied, the depletion of ions in the nanochannel makes the profile of ions, and therefore, their interaction with the nanochannel surface insensitive to the nanochannel geometry. Therefore, the ICR factor R_f exhibits a local maximum as γ varies. R_f also exhibits a local maximum as the ratio λ (=length of smaller channel/total channel length) varies. This local maximum occurs at a small value of λ (i.e., the smaller segment of the nanochannel is short). If λ is large, ions accumulate appreciably in the smaller segment of the nanochannel making the difference between the current at a positively applied voltage bias and that at a negatively applied voltage biases insignificant so that ICR is not significant. As λ gets small, because there is more space for ion enrichment/depletion, R_f becomes large. However, if λ is too small, the EDL in the smaller segment of a nanochannel is unable to confine enough amount of



ions to help accumulating ions in its larger segment so that ICR is insignificant. The variation of the solution pH also leads to a local maximum in R_f . This can be explained by the variations in the conductivity and the current at different applied voltage biases. The current in the preferential direction is nearly proportional to the extent of the deviation of pH from IEP, but it is not the case in the opposite direction of the current. In the latter, the current increases first with the degree of deviation of pH from IEP, but becomes insensitive to that deviation if pH is sufficiently far from IEP. The results gathered in our study provide desirable and necessary information for both the design of relevant devices and the optimization of their performance.

References



- [1] Liu, Q., Xiao, K., Wen, L. P., Lu, H., Liu, Y. H., Kong, X. Y., Xie, G. H., Zhang, Z., Bo, Z. S., Jiang, L., *J. Am. Chem. Soc.* 2015, *137*, 11976-11983.
- [2] Zhang, H. C., Tian, Y., Hou, J., Hou, X., Hou, G. L., Ou, R. W., Wang, H. T., Jiang, L., *Acs Nano* 2015, *9*, 12264-12273.
- [3] Xiao, K., Chen, L., Zhang, Z., Xie, G. H., Li, P., Kong, X. Y., Wen, L. P., Jiang, L., *Angew. Chem. Int. Ed. Engl.* 2017, *56*, 8168-8172.
- [4] Xie, G. H., Xiao, K., Zhang, Z., Kong, X. Y., Liu, Q., Li, P., Wen, L. P., Jiang, L., *Angew. Chem. Int. Ed. Engl.* 2015, *54*, 13664-13668.
- [5] Plett, T. S., Cai, W. J., Le Thai, M., Vlassiouk, I. V., Penner, R. M., Siwy, Z. S., *J. Phys. Chem. C* 2017, *121*, 6170-6176.
- [6] Zheng, Y. B., Zhao, S., Cao, S. H., Cai, S. L., Cai, X. H., Li, Y. Q., *Nanoscale* 2017, *9*, 433-439.
- [7] Balme, S., Ma, T. J., Balanzat, E., Janot, J. M., *J. Membr. Sci.* 2017, *544*, 18-24.
- [8] Siria, A., Poncharal, P., Bianco, A. L., Fulcrand, R., Blase, X., Purcell, S. T., Bocquet, L., *Nature* 2013, *494*, 455-458.
- [9] Corry, B., *Energy Environ. Sci.* 2011, *4*, 751-759.
- [10] Heiranian, M., Farimani, A. B., Aluru, N. R., *Nat. Commun.* 2015, *6*, 8616.



- [11] Ma, Y., Yeh, L. H., Lin, C. Y., Mei, L. J., Qian, S. Z., *Anal. Chem.* 2015, 87, 4508-4514.
- [12] Schoch, R. B., Han, J. Y., Renaud, P., *Rev. Mod. Phys.* 2008, 80, 839-883.
- [13] Zangle, T. A., Mani, A., Santiago, J. G., *Chem. Soc. Rev.* 2010, 39, 1014-1035.
- [14] Yeh, L. H., Zhang, M., Qian, S., Hsu, J. P., Tseng, S., *J. Phys. Chem. C* 2012, 116, 8672-8677.
- [15] Zeng, Z. P., Yeh, L. H., Zhang, M. K., Qian, S. Z., *Nanoscale* 2015, 7, 17020-17029.
- [16] Vlassiouk, I., Smirnov, S., Siwy, Z., *Nano Lett.* 2008, 8, 1978-1985.
- [17] White, H. S., Bund, A., *Langmuir* 2008, 24, 2212-2218.
- [18] Siwy, Z. S., *Adv. Funct. Mater.* 2006, 16, 735-746.
- [19] Chander, M., Kumar, R., Kumar, S., Kumar, N., Chakarvarti, S. K., *Dig. J. Nano. Bio.* 2018, 13, 13-21.
- [20] Zhang, H. C., Hou, X., Zeng, L., Yang, F., Li, L., Yan, D. D., Tian, Y., Jiang, L., *J. Am. Chem. Soc.* 2013, 135, 16102-16110.
- [21] Xiao, K., Chen, L., Xie, G. H., Li, P., Kong, X. Y., Wen, L. P., Jiang, L., *Nanoscale* 2018, 10, 6850-6854.
- [22] Siwy, Z., Heins, E., Harrell, C. C., Kohli, P., Martin, C. R., *J. Am. Chem. Soc.* 2004, 126, 10850-10851.



[23] Xiao, K., Li, P., Xie, G. H., Zhang, Z., Wen, L. P., Jiang, L., *Rsc Advances* 2016, 6, 55064-55070.

[24] Tseng, S. J., Lin, S. C., Lin, C. Y., Hsu, J. P., *J. Phys. Chem. C* 2016, 120, 25620-25627.

[25] Ali, M., Yameen, B., Cervera, J., Ramirez, P., Neumann, R., Ensinger, W., Knoll, W., Azzaroni, O., *J. Am. Chem. Soc.* 2010, 132, 8338-8348.

[26] Kalman, E. B., Vlassioug, I., Siwy, Z. S., *Adv. Mater.* 2008, 20, 293-297.

[27] Liu, N. N., Jiang, Y. N., Zhou, Y. H., Xia, F., Guo, W., Jiang, L., *Angew. Chem. Int. Ed. Engl.* 2013, 52, 2007-2011.


[28] Chander, M., Kumar, R., Kumar, S., Kumar, N., Chakarvarti, S. K., *Nano* 2018, 13, 1850011.

[29] Nasir, S., Ali, M., Ramirez, P., Gomez, V., Oschmann, B., Muench, F., Tahir, M. N., Zentel, R., Mafe, S., Ensinger, W., *ACS Appl. Mater. Interfaces* 2014, 6, 12486-12494.

[30] Tagliazucchi, M., Rabin, Y., Szleifer, I., *ACS Nano* 2013, 7, 9085-9097.

[31] Al Sulaiman, D., Cadinu, P., Ivanov, A. P., Edel, J. B., Ladame, S., *Nano Lett.* 2018, 18, 6084-6093.

[32] Ali, M., Ramirez, P., Nguyen, H. Q., Nasir, S., Cervera, J., Mafe, S., Ensinger, W., *Acs Nano* 2012, 6, 3631-3640.

- 
- [33] Han, K. Y., Heng, L. P., Wen, L. P., Jiang, L., *Nanoscale* 2016, 8, 12318-12323.
- [34] Lin, T. W., Hsu, J. P., Lin, C. Y., Tseng, S., *J. Phys. Chem. C* 2019, 123, 12437-12443.
- [35] Cao, L. X., Guo, W., Wang, Y. G., Jiang, L., *Langmuir* 2012, 28, 2194-2199.
- [36] Lan, W. J., Holden, D. A., White, H. S., *J. Am. Chem. Soc.* 2011, 133, 13300-13303.
- [37] Apel, P. Y., Blonskaya, I. V., Dmitriev, S. N., Orelovitch, O. L., Presz, A., Sartowska, B. A., *Nanotechnology* 2007, 18, 305302.
- [38] Li, J., Stein, D., McMullan, C., Branton, D., Aziz, M. J., Golovchenko, J. A., *Nature* 2001, 412, 166-169.
- [39] Storm, A. J., Chen, J. H., Ling, X. S., Zandbergen, H. W., Dekker, C., *Nat. Mater.* 2003, 2, 537-540.
- [40] Gamble, T., Decker, K., Plett, T. S., Pevarnik, M., Pietschmann, J. F., Vlassiouk, I., Aksimentiev, A., Siwy, Z. S., *J. Phys. Chem. C* 2014, 118, 9809-9819.
- [41] Hsu, J. P., Lin, T. W., Lin, C. Y., Tseng, S., *J. Phys. Chem. C* 2017, 121, 28139-28147.
- [42] Kong, Y., Fan, X., Zhang, M. H., Hou, X., Liu, Z. Y., Zhai, J., Jiang, L., *ACS Appl. Mater. Interfaces* 2013, 5, 7931-7936.
- [43] Li, C. Y., Wu, Z. Q., Yuan, C. G., Wang, K., Xia, X. H., *Anal. Chem.* 2015, 87, 8194-8202.
- [44] Hsu, J. P., Chen, Y. C., Chen, Y. M., Tseng, S., *J. Taiwan Inst. Chem. Eng.* 2018, 93,



142-149.

[45] Kovarik, M. L., Zhou, K. M., Jacobson, S. C., *J. Phys. Chem. B* 2009, *113*, 15960-15966.

[46] Apel, P. Y., Blonskaya, I. V., Orelovitch, O. L., Ramirez, P., Sartowska, B. A., *Nanotechnology* 2011, *22*, 175302

[47] Schonenberger, C., vanderZande, B. M. I., Fokkink, L. G. J., Henny, M., Schmid, C., Kruger, M., Bachtold, A., Huber, R., Birk, H., Staufer, U., *J. Phys. Chem. B* 1997, *101*, 5497-5505.

[48] Mara, A., Siwy, Z., Trautmann, C., Wan, J., Kamme, F., *Nano Lett.* 2004, *4*, 497-501.

[49] Lee, W., Park, S. J., *Chem. Rev.* 2014, *114*, 7487-7556.

[50] Yeh, L. H., Chen, F., Chiou, Y. T., Su, Y. S., *Small* 2017, *13*.

[51] Kosmulski, M., *J. Colloid Interface Sci.* 2004, *275*, 214-224.

[52] Albrecht, T., Gibb, T., Nuttall, P., *Engineered Nanopores for Bioanalytical Applications*, William Andrew Publishing, United States 2013, pp. 1-30.

[53] Cervera, J., Schiedt, B., Neumann, R., Mafe, S., Ramirez, P., *J. Chem. Phys.* 2006, *124*, 104706

[54] Hsu, J. P., Wu, H. H., Lin, C. Y., Tseng, S., *Anal. Chem.* 2017, *89*, 3952-3958.

[55] Pietschmann, J. F., Wolfram, M. T., Burger, M., Trautmann, C., Nguyen, G.,

Pevarnik, M., Bayer, V., Siwy, Z., *Phys. Chem. Chem. Phys* 2013, 15, 16917-16926.



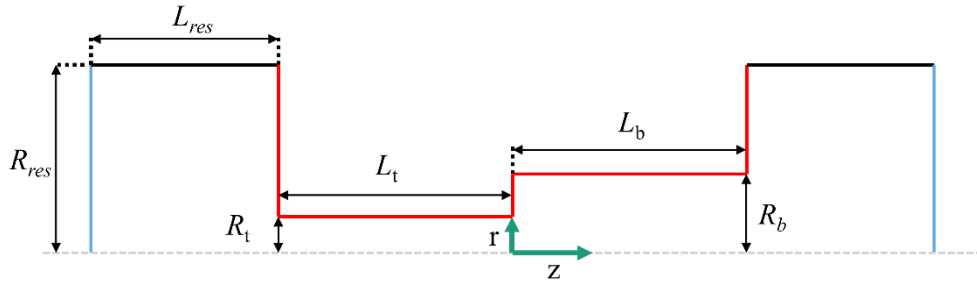


Figure 1-1. A nanochannel comprises two series connected cylindrical nanochannels, the length and the radius of the base end section of the nanochannel are L_b and R_b , respectively, and L_t and R_t are the length and the radius of the tip end section of the nanochannel

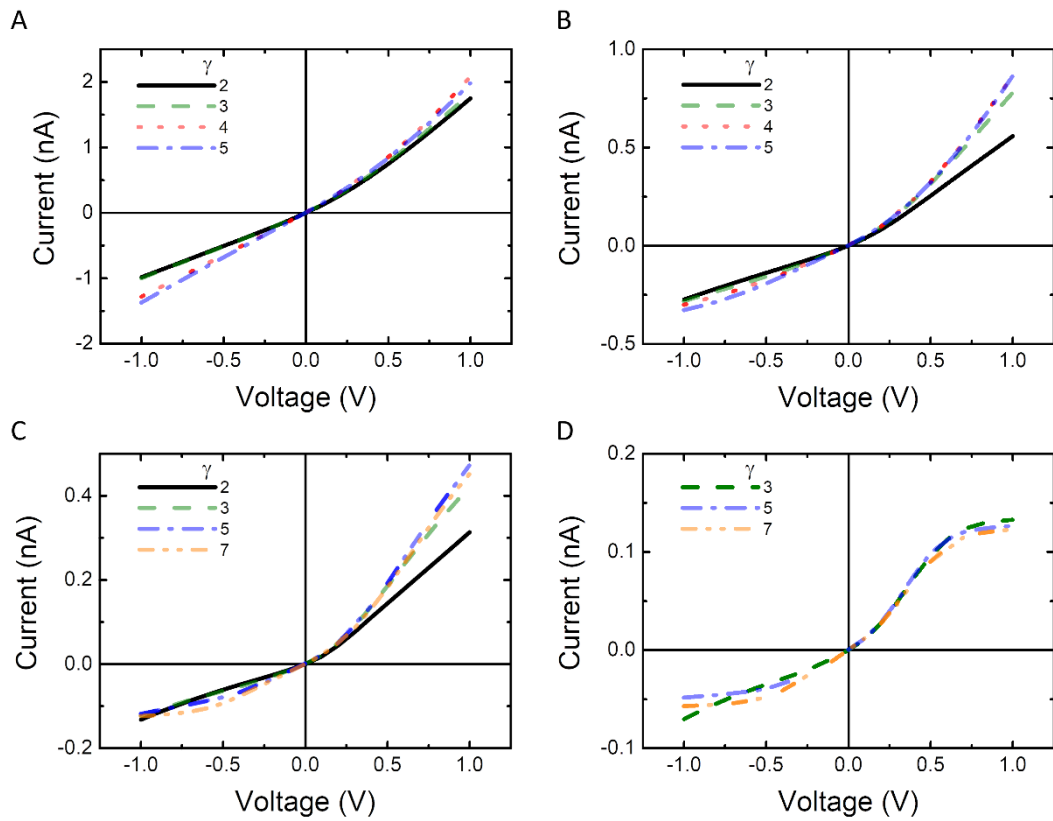


Figure 1-2. Simulated $I-V_{app}$ curves for various combinations of the bulk salt concentration C_0 and the segment radii ratio γ at pH 4 and $\lambda=0.5$. (A) $C_0=100$ mM, (B) $C_0=10$ mM, (C) $C_0=1$ mM, (D) $C_0=0.1$ mM KCl.

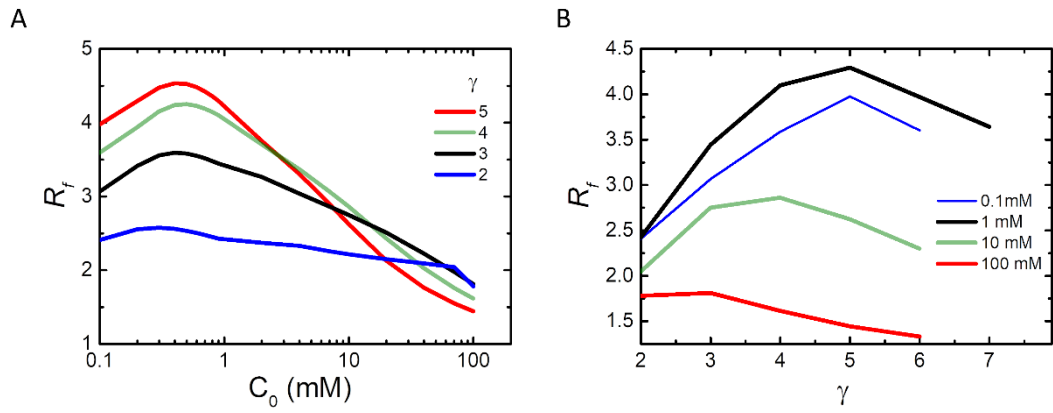


Figure 1-3. (A) Variation of R_f with the bulk salt concentration C_0 for various values of γ . (B) Variation of R_f with the segment radii ratio γ for various levels of the bulk salt concentration C_0 . pH is 4 and $\lambda=0.5$ in both cases.

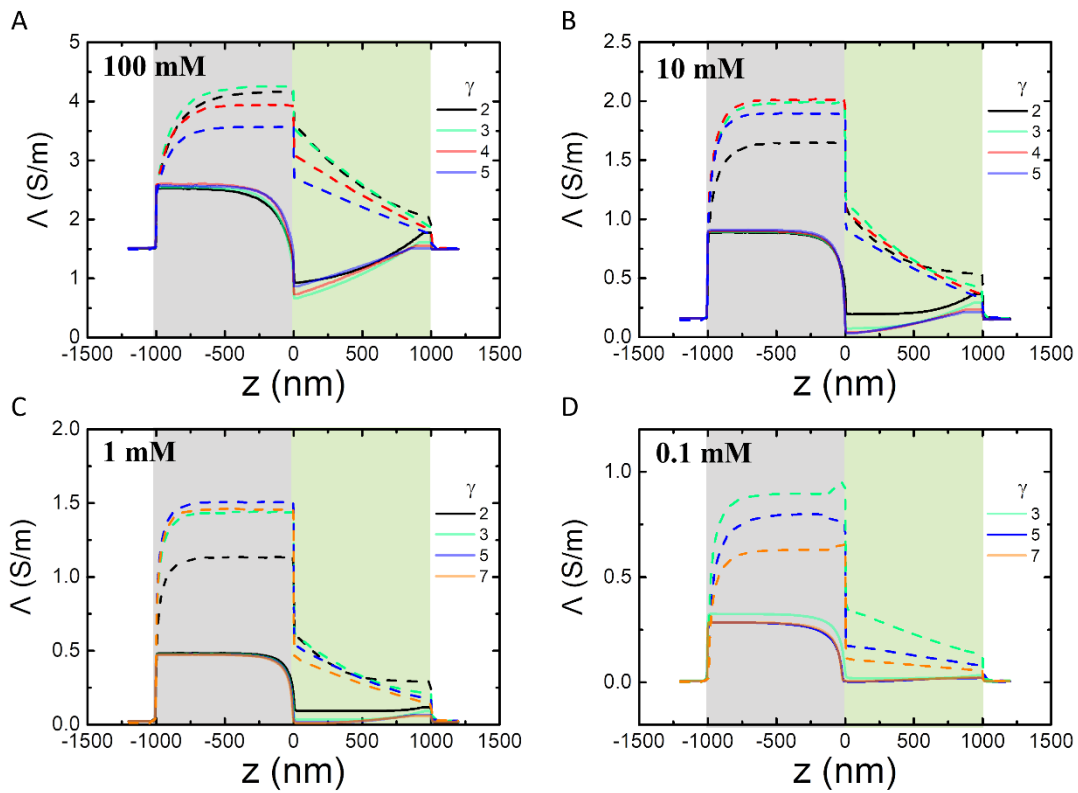
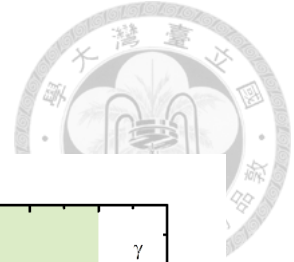


Figure 1-4. Axial variation in the cross-sectional averaged ionic conductivity for various values of γ at pH 4 and $\lambda=0.5$. (A) $C_0=100$ mM, (B) $C_0=10$ mM, (C) $C_0=1$ mM, (D) $C_0=0.1$ mM KCl. Solid curves: $V_{app}=-1$ V; dash curves: $V_{app}=+1$ V.

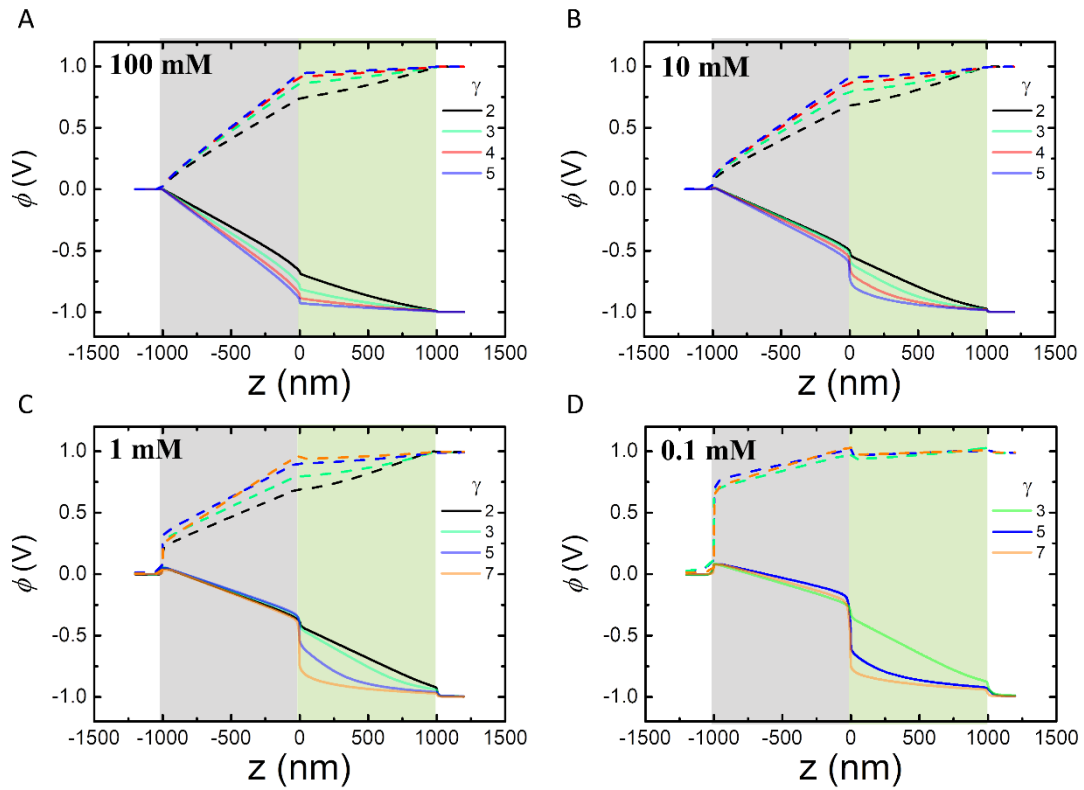


Figure 1-5. Axial variation in the cross-sectional averaged electric potential for various values of γ at pH 4 and $\lambda=0.5$. (A) $C_0=100$ mM, (B) $C_0=10$ mM, (C) $C_0=1$ mM, (D) $C_0=0.1$ mM. Solid curves: $V_{\text{app}}=-1$ V; dash curves: $V_{\text{app}}=+1$ V. Shaded areas denote the nanochannel interior.

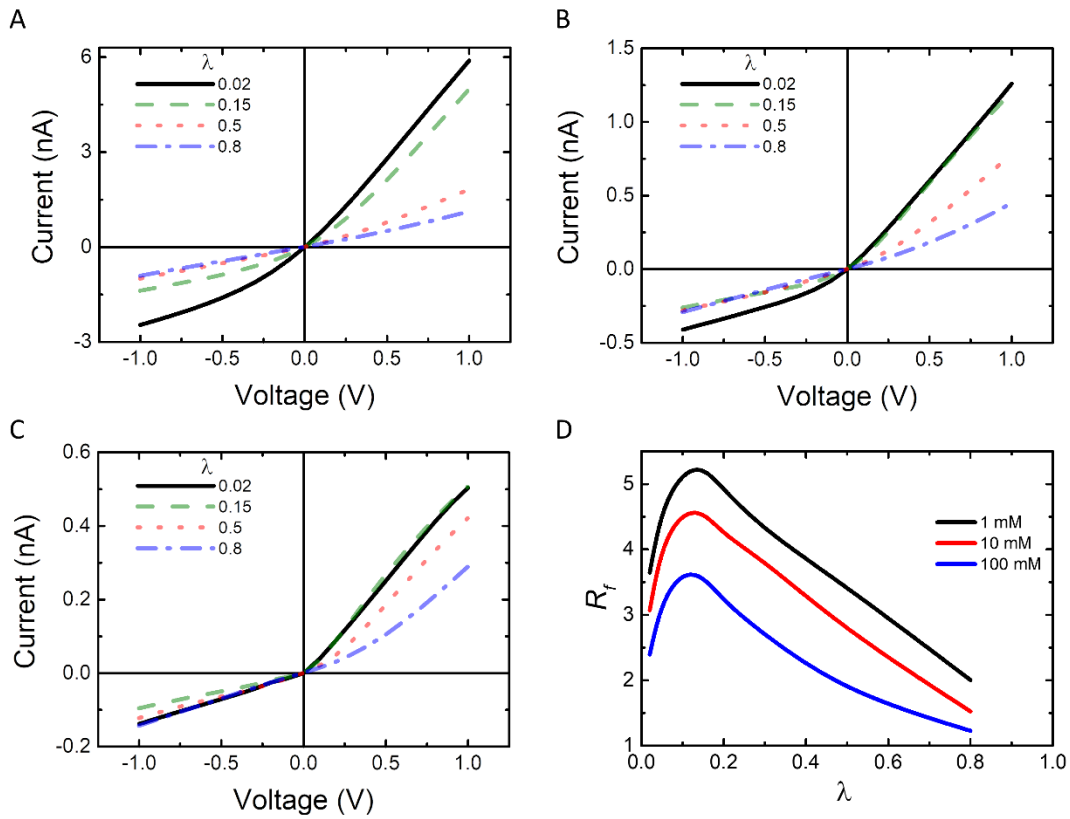
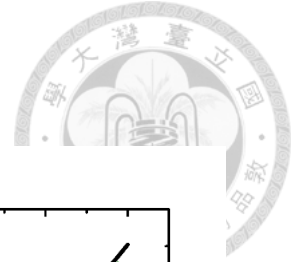


Figure 1-6. Simulated $I-V_{app}$ curves for various combinations of the bulk salt concentration C_0 and the segment length ratio λ at pH 4 and $\gamma=3$. (A) $C_0=100$ mM, (B) $C_0=10$ mM, (C) $C_0=1$ mM KCl. (D) Variation of R_f with the segment length ratio λ for various levels of the bulk salt concentration C_0 .

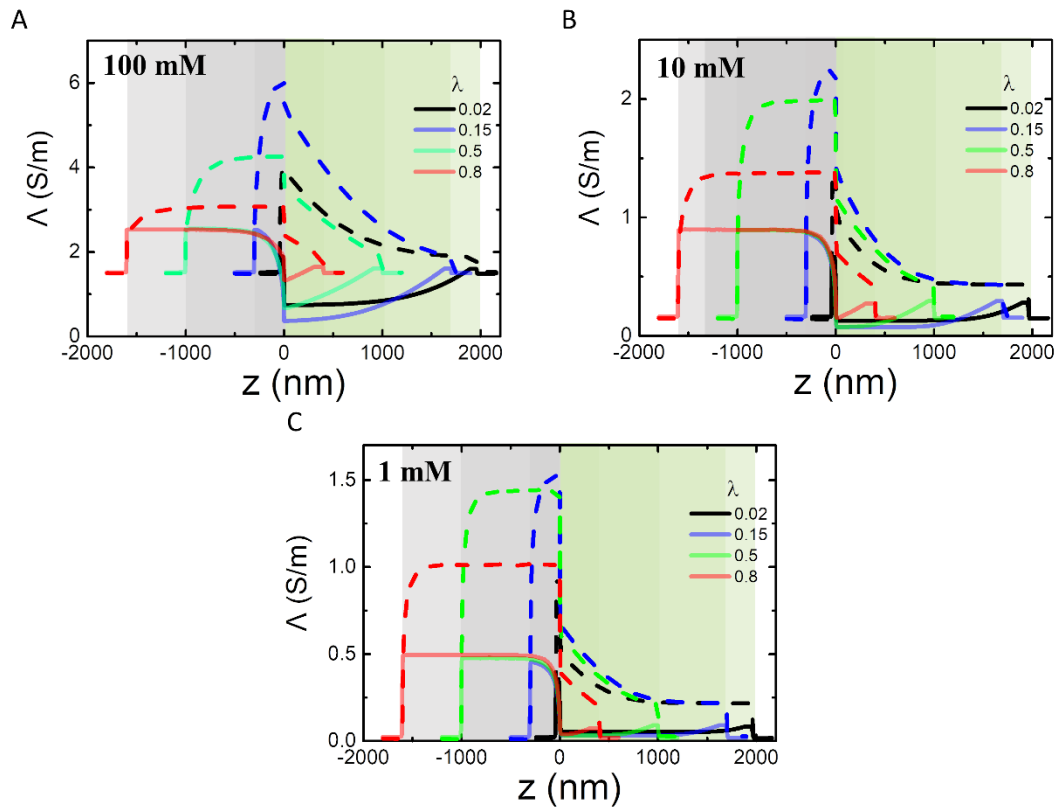
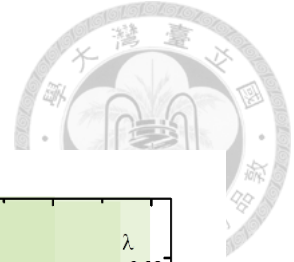


Figure 1-7. Axial variation in the cross-sectional averaged ionic conductivity for various values of λ at pH 4 and $\gamma=3$. (A) $C_0=100$ mM, (B) $C_0=10$ mM, (C) $C_0=1$ mM KCl. Solid curves: $V_{app}=-1$ V; dashed curves: $V_{app}=+1$ V.

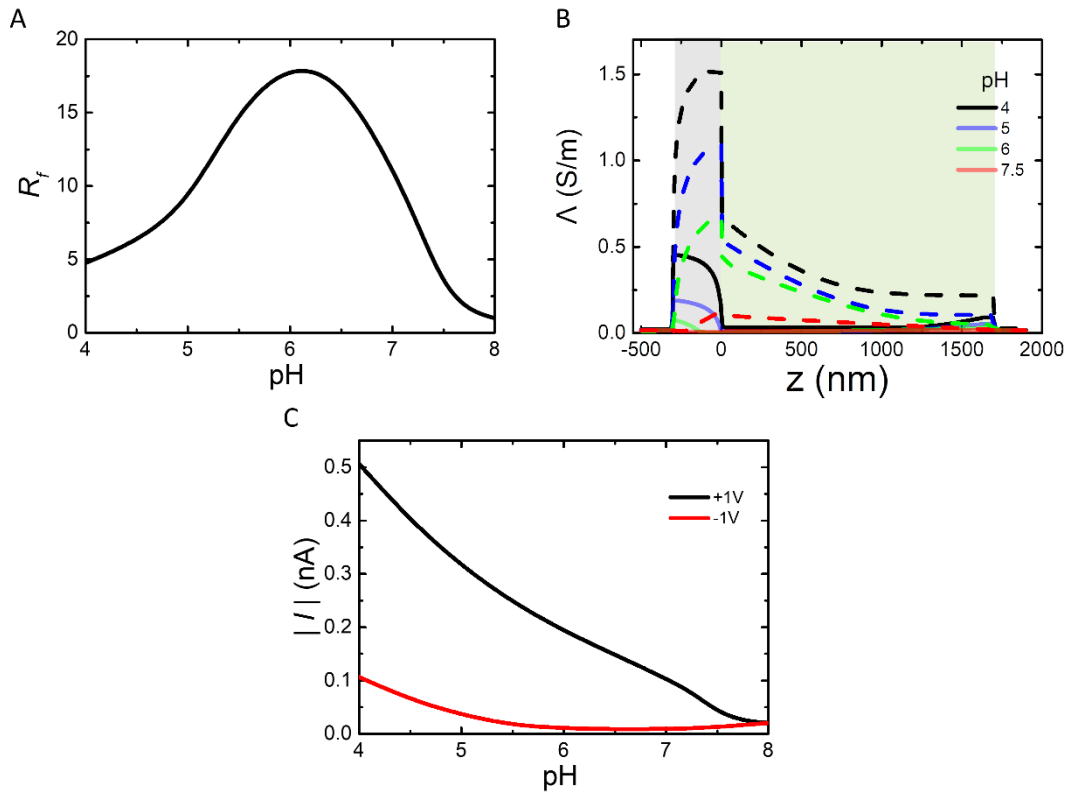


Figure 1-8. (A) Variation of the ICR factor R_f with pH. (B) Axial variation in the cross-sectional averaged ionic conductivity for various values of pH. Solid curves: $V_{app}=+1$ V; dashed curves: $V_{app}=-1$ V. (C) Variation of $|I|$ with pH at $V_{app}=\pm 1$ V. Parameters assumed are $\lambda=0.15$ and $\gamma=3$ and $C_0=1$ mM KCl.

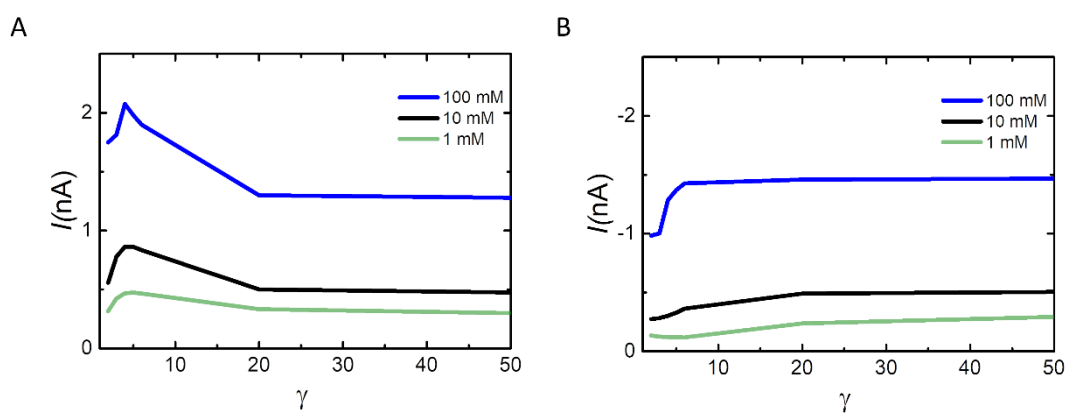
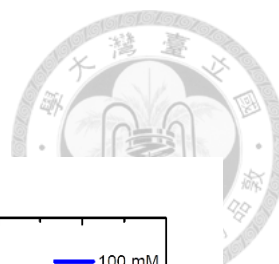


Figure 1-S1. Variation of the ionic current I with the segment radii ratio γ at various levels of the bulk salt concentration C_0 at $\lambda=0.5$. (A) $V_{app}=+1$ V, (B) $V_{app}=-1$ V.

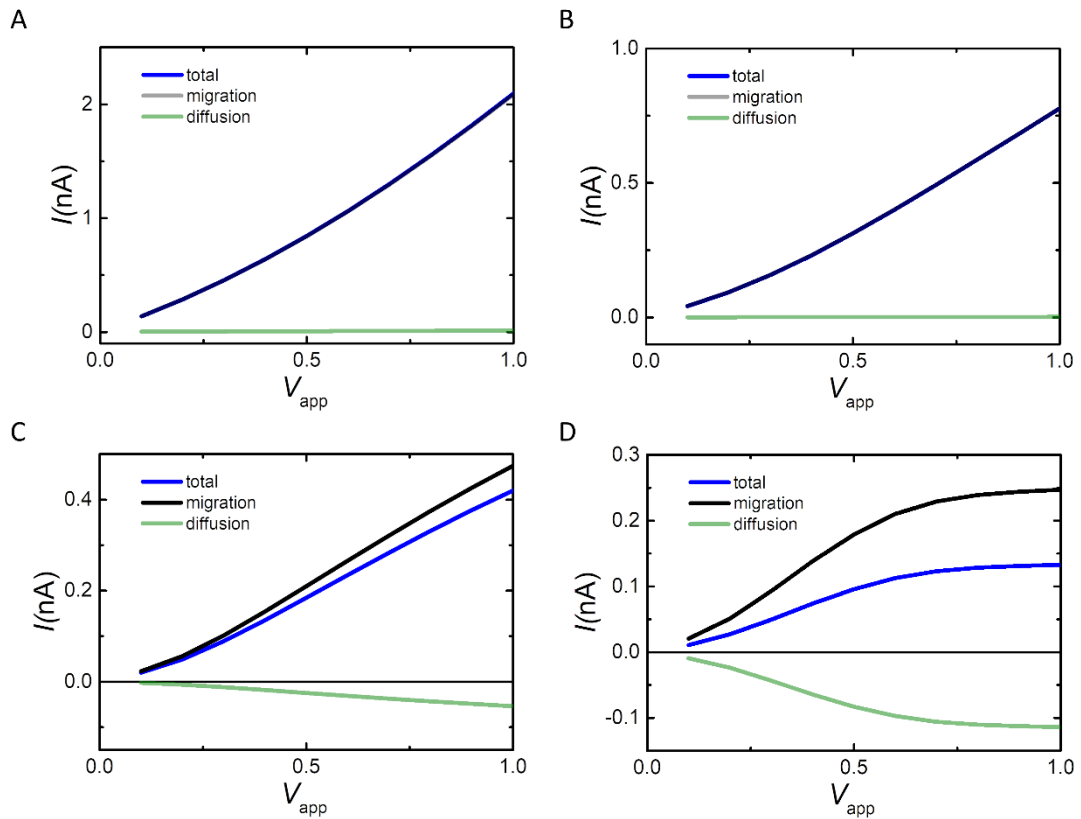


Figure 1-S2. Simulated I - V_{app} curves for various combinations of the bulk salt concentration C_0 at pH 4 and $\gamma=3$. (A) $C_0=100$ mM, (B) $C_0=10$ mM, (C) $C_0=1$ mM, (D) $C_0=0.1$ mM KCl. The contributions of the migration and the diffusion terms in eq (3) to I are also presented.

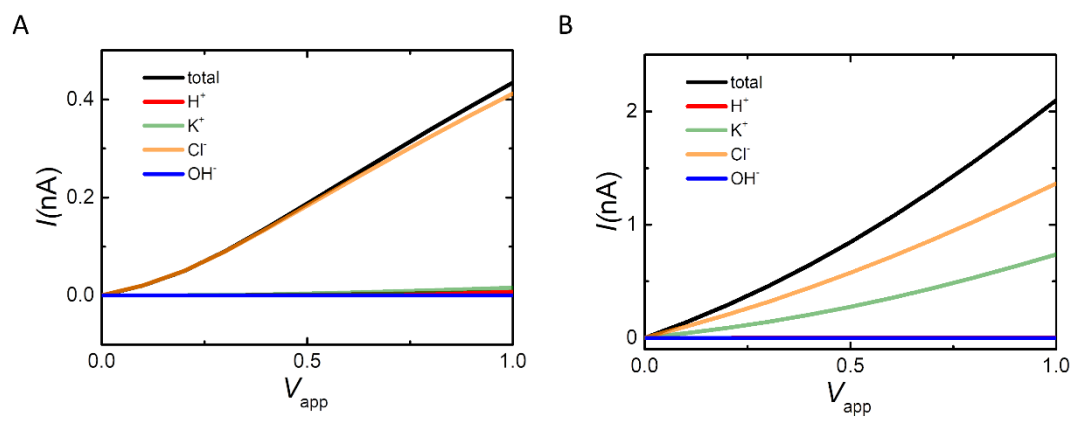


Figure 1-S3. Simulated I - V_{app} curves for various combinations of ion species at pH 4, $\gamma=3$ and $\lambda=0.5$. (A) $C_0=1$ mM, (B) $C_0=100$ mM.

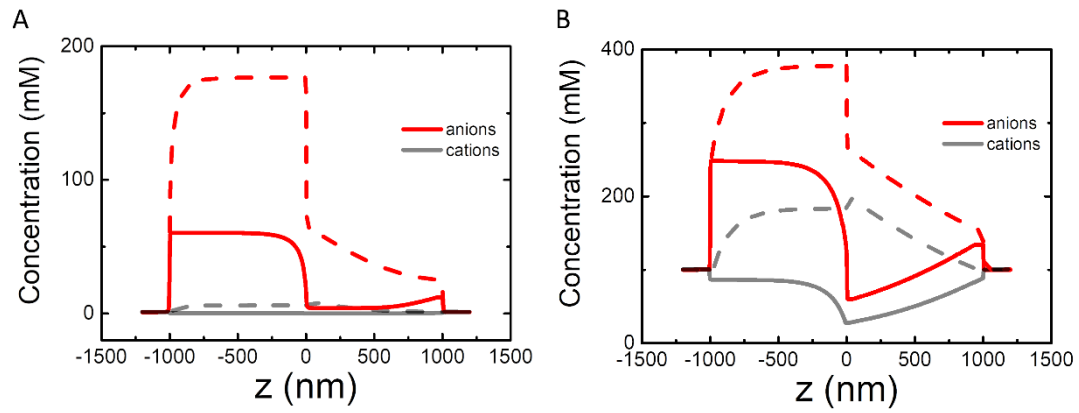
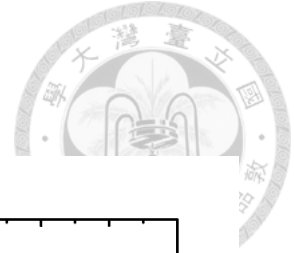


Figure 1-S4. Axial variation in the cross-sectional averaged concentration for both cations and anions at pH 4, $\gamma=3$ and $\lambda=0.5$. (A) $C_0=1$ mM, (B) $C_0=100$ mM KCl. Solid curves: $V_{app}=-1$ V; dashed curves: $V_{app}=+1$ V.

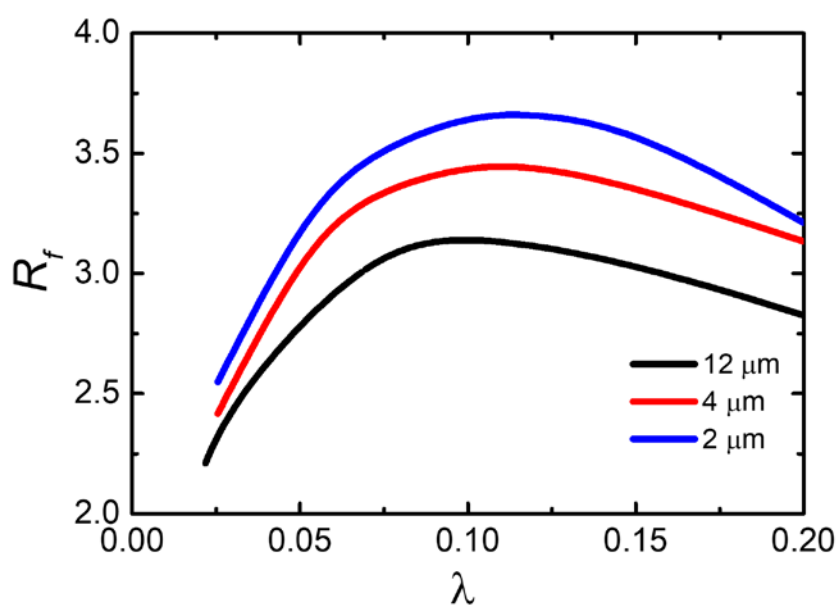


Figure 1-S5. Variation of R_f with the segment length ratio λ for various levels of L_{total} at pH 4, $\gamma=3$ and $C_0=100$ mM KCl.

Chapter 2



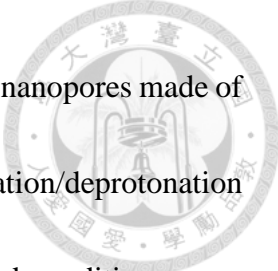
Electrokinetic Behavior of a pH-regulated, Dielectric Cylindrical Nanopore



2-1. Introduction

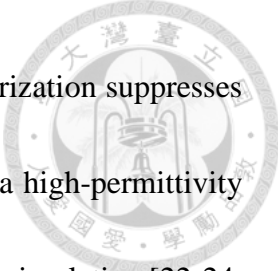
Due to its versatile potential applications in fields such as biosensing [1-3], nanofluidic circuits [4-6], and energy conversion [7-9], ion transport through nanometer-sized channels has been studied extensively in the last decades. It is known that the behavior of ionic conductance in a nanoscaled space can be quite different from that in a regular scaled space [10]. For example, the current through a nanopore can show a non-linear dependence on the salt concentration. This non-linear behavior is attributed to the presence of an electrical double layer (EDL) near a charged surface and a large surface-to-volume ratio of a nanoscaled system. These properties yield interesting and important phenomena including, for instance, ion concentration polarization (ICP) [11, 12] and ion selectivity [13, 14]. Since the thickness of EDL (also known as Debye length) is comparable to the linear size of a nanoscaled system (e.g., radius of a nanopore), its electrokinetic behavior rests largely on the degree of EDL overlapping inside it.

To understand/elaborate the mechanisms involved in the ionic transport in a nanopore/nanochannel, a consider amount of theoretical efforts has been made. Assuming constant charge density, Cervera et al [15], for example, model the ionic transport in a synthetic conical nanopore by Poisson and Nernst-Planck (PNP) equations. A constant surface charge density model is usually adopted in earlier studies [16-18], for simplicity.



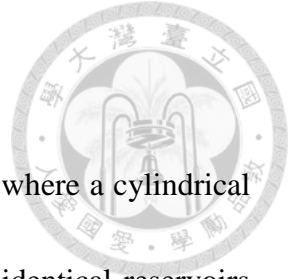
Recent analyses take account of the pH-regulated nature of solid-state nanopores made of metal oxides or polymeric materials, where the surface protonation/deprotonation reactions occur in an aqueous environment make the surface charged conditions more complicated but realistic. For instance, Yeh et al. [19] modeled the ion transport behavior of cylindrical silica nanopore by considering pH-regulated charged conditions. They showed with experimental data that the surface charge density of the nanopore can be spatially dependent. Latter study also revealed that H^+ (OH^-) plays a crucial role at a low (high) level of pH [20]. The control/regulation of the surface charge leaves substantial interests to explore, thereby leading to lots of possible nanofluidic devices.

The dielectric nature of the membrane materials used to prepare a nanopore can also influence appreciably its electrokinetic performance. If an external electric field is applied to a nanopore made of dielectric material, a reverse electric field coming from surface polarization is established inside the membrane, thereby influencing the ionic transport inside. For example, dielectric exclusion, an ionic partitioning phenomenon occurring in nanofiltration arises from that the dielectric constant of an aqueous solution is much larger than that of the membrane used [21]. It was found that the dielectric properties of a calcium channel is capable of influencing its binding selectivity [22-24]. Recent studies also demonstrated that ion mobility can be modulated by the dielectric properties of



membrane substrate [25-27]. This was explained by that surface polarization suppresses ion mobility near a low-permittivity surface, but enhances that near a high-permittivity surface. Reported theoretical results are mainly based on Monte Carlo simulation [22-24, 28] and molecular dynamics [25-27], where detailed information about the number of ions near a surface and their local profile can be retrieved. Unfortunately, due to computational limits, these approaches are inapplicable to evaluate the ionic current through a nanopore, the most convenient measurable quantity for describing its electrokinetic behavior. In contrast, the ionic current is readily retrievable from a continuum-based model [15, 19, 29]. Qian et al. [30], for example, applied such model to show that the ionic current rectification (ICR) behavior of a conical nanopore can be tuned by the permittivity of the membrane material.

Up to now, a comprehensive understanding of the polarization effect associated with dielectric materials and the underlying mechanisms have not been reported on the basis of a continuum model. The present theoretical study is aimed to explore these by considering a cylindrical nanopore having a pH-regulated surface. The dielectric constant of the nanopore material, the nanopore dimension, the bulk salt concentration, and the solution pH are examined for their influence on the electrokinetic transport properties of the system under consideration.



2-2. Theoretical Model

Let us consider the system shown schematically in Figure 2-1, where a cylindrical nanochannel of length L_n and radius R_n is connected to two large, identical reservoirs filled with an aqueous salt solution. To improve the computation efficiency, a computation domain Ω is defined which comprises the nanochannel and a cylindrical domain of length L_r and R_r in each reservoir. The upper reservoir is grounded, and a potential bias V_0 is applied to the lower one. The physicochemical properties on the liquid boundaries of Ω reach essentially the corresponding bulk values. For convenience, Ω is also divided into the fluid domain Ω_f and the membrane domain Ω_m . The cylindrical coordinates are adopted with the origin placed at the nanochannel center. Due to axial symmetry, only the (r, z) domain needs be considered.

Assuming that the liquid phase is an incompressible Newtonian fluid and the system under consideration is at a pseudo-steady state, then the electric, the concentration, and the flow fields can be described by the following equations.

(i) Navier-Stokes and continuity equations

If we let \mathbf{u} be the fluid velocity, and p , μ , and φ be the hydrodynamic pressure, the fluid viscosity, and the electric potential, respectively, then the flow field can be described by



$$-\nabla p + \mu \nabla^2 \mathbf{u} - \rho_f \nabla \varphi = \mathbf{0} \text{ in } \Omega_f \quad (1)$$

$$\nabla \cdot \mathbf{u} = 0 \text{ in } \Omega_f \quad (2)$$

$\rho_f = F \sum_{i=1}^N z_i C_i$ is the space charge density in the liquid phase with F being Faraday constant, z_i and C_i the valence and the concentration of ionic species i , and N the kinds of ionic species. Note that because the Reynolds number is small in nanofluidics, the inertial terms in the Navier-Stokes equation is neglected.

(ii) Poisson-Nernst-Planck equation

The spatial variation in the electric potential in the liquid domain, φ , and that in the membrane domain, Ψ , are described by

$$-\varepsilon_0 \varepsilon_f \nabla^2 \varphi = \rho_f \text{ in } \Omega_f \quad (3)$$

$$-\varepsilon_0 \varepsilon_m \nabla^2 \Psi = \rho_m \text{ in } \Omega_m \quad (4)$$

ε_0 is the absolute permittivity of a vacuum, ε_f and ε_m are relative permittivity of the fluid and that of membrane, and ρ_m is the space charge density in the membrane domain, respectively. Since the membrane domain is free of charge, $\rho_m = 0$ in eq (4), that is, it is a Laplace equation.

The ionic flux of the i th ionic species, \mathbf{N}_i , can be expressed as

$$\mathbf{N}_i = \mathbf{u} C_i - D_i \nabla C_i - z_i \frac{D_i}{RT} F C_i \nabla \varphi, i = 1, 2, \dots, N \text{ in } \Omega_f \quad (5)$$

D_i is the diffusivity of ionic species i , T the absolute temperature, and R universal gas



constant. The terms on the right-hand side of eq (5) denote the convective, diffusive, and electromigrative contributions to \mathbf{N}_i , respectively. The conservation of ionic species i yields the Nernst-Planck equation below:

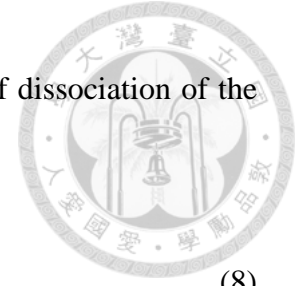
$$\nabla \cdot \mathbf{N}_i = 0 \quad (6)$$

We assume the following. (i) The nanochannel walls (surfaces 4, 5, 6) are non-slip ($\mathbf{u}=\mathbf{0}$) and ion-impenetrable ($\mathbf{n} \cdot \mathbf{N}_i = 0$). The surface charge density σ can be expressed as

$$\mathbf{n} \cdot (-\varepsilon_0 \varepsilon_f \nabla \varphi) + \mathbf{n} \cdot (-\varepsilon_0 \varepsilon_m \nabla \Psi) = \sigma \quad (7)$$

\mathbf{n} is the unit outer normal vector. (ii) The side boundaries of the computation domain in the two reservoirs (surfaces 3 and 7) are slip, free of fixed charge ($-\mathbf{n} \cdot \nabla \varphi=0$), and have no net normal ionic flux ($\mathbf{n} \cdot \mathbf{N}_i=0$). The side boundary of the membrane (surface 9) is free of fixed charge ($-\mathbf{n} \cdot \nabla \varphi=0$). (iii) The end surfaces of the computation domain in the two reservoirs (surfaces 2 and 8) are sufficiently far from the nanochannel so that the ionic concentration there reaches the bulk value (i. e., $C_i=C_{i0}$). In addition, no external pressure gradient is applied ($p=0$). The top-end surface (surface 2) is grounded ($\varphi=0$), and a voltage bias ($\varphi=V_0$) is applied to the bottom-end surface (surface 8). (iv) The axial symmetric condition is applied to all dependent variables. The boundary conditions associated with the governing eqs (1)-(6) are summarized in Table 2-1.

Suppose that the nanochannel surface has carboxyl groups ($\sim\text{COOH}$) with site



density Γ_t so that its charge density σ depends upon the degree of dissociation of the reaction below:



If we let $[\text{H}^+]_s$ be the surface concentration of H^+ and K_A be the equilibrium constant, it can be shown that [20]

$$\sigma = -F\Gamma_t \frac{K_A}{K_A + [\text{H}^+]_s} \quad (9)$$

K_A is ca. 4, and Γ_t ranges from 1 to 1.5 nm⁻². [31-33]

We assume that the background salt is KCl, and the solution pH is adjusted by introducing HCl and KOH, implying that four kinds of ionic species are present in the system (i.e., $N=4$). Let C_b and $[\text{H}^+]_0$ be the background concentration of KCl and that of H^+ , respectively, and C_{10} , C_{20} , C_{30} , and C_{40} denote the bulk molar concentrations of H^+ , K^+ , Cl^- , and OH^- , respectively. The following conditions need be satisfied [34] :

$C_{10} = 10^{-\text{pH}+3}$, $C_{20} = C_b$, $C_{30} = C_b + 10^{-\text{pH}+3} - 10^{-(14-\text{pH})+3}$, and $C_{40} = 10^{-(14-\text{pH})+3}$ for $\text{pH} \leq 7$; $C_{10} = 10^{-\text{pH}+3}$, $C_{20} = C_b - 10^{-\text{pH}+3} + 10^{-(14-\text{pH})+3}$, $C_{30} = C_b$, and $C_{40} = 10^{-(14-\text{pH})+3}$ for $\text{pH} > 7$.

If we let S be the cross-sectional area of the nanochannel, the ionic current I through it can be calculated by

$$I = \int F \sum_{i=1}^4 (z_i N_i) \cdot \mathbf{n} dS \quad (10)$$



Define the ionic conductance G as

$$G = I/V_0 \quad (11)$$

COMSOL Multiphysics (version 5.4) is adopted to solving the governing equations subject to the boundary conditions summarized in Table 1. To ensure the results obtained are reliable, mesh independence is checked throughout the solution procedure with a finer mesh employed near the nanochannel surface. Typically, using ca. 650,000 meshes is sufficient for obtaining reliable and accurate results. Code verification is also conducted by solving the problem considered by Smeets. et al. [10]. Figure 2-S1 of the Supporting Information reveals that the performance of the present model and the solution procedure are satisfactory.

2-3. Results and Discussion

To simulate the behavior of the present system under various conditions, we assume: $T=300$ K, $\rho=1 \times 10^3$ kg/m³, $\mu=1 \times 10^{-3}$ Pa·s, and $\varepsilon_f=80$. The diffusion coefficients of H⁺, K⁺, Cl⁻, and OH⁻ are 9.31×10^{-9} , 1.96×10^{-9} , 2.03×10^{-9} , and 5.30×10^{-9} m²/s, respectively [19]. In addition, $K_A=4$ and $\Gamma_t=1$ nm⁻² [31-33]. The synthetic nanopores are usually made of dielectric materials such as silicon compound, alumina, polymer, and protein, the relative permittivity of these materials are smaller than 80 [22, 35, 36]. Therefore, the

relative permittivity of nanopore material ϵ_m ranges from 0 to 80 in our study.

Figure 2-S2 shows the typical current-voltage curve at pH 4 for various levels of ϵ_m .

The non-Ohmic dependence of the ionic current I on the applied voltage bias V_0 observed at high ϵ_m arises from the polarization of the membrane material. The degree of this polarization is proportional to the level of V_0 as reported [30, 37]. For illustration, V_0 is fixed at -1V in subsequent discussion.

2-3-1. Influence of nanopore dimension

As shown in Figure 2-2(a), the nanopore conductance G decreases with increasing nanopore length L_n , which is analytically predicted and demonstrated both experimentally and numerically in previously studies [29, 38, 39]. In addition, even ϵ_m is large, G still increases with decreasing nanopore length, which is expected since the longer the nanopore the greater its resistance. To quantify the influence of ϵ_m on G , we define the conductance ratio $n = G(\epsilon_m=80)/G(\epsilon_m=0)$. As can be seen in the insert of Figure 2-2(a), the influence of ϵ_m becomes significant as L_n gets shorter than 50 nm. Note that if L_n is shorter slightly than ca. 100 nm, n is slightly smaller than unity. If L_n is longer ca. 500 nm, the influence of ϵ_m on G becomes insignificant. Figure 2-2(b) reveals that if the nanopore is sufficiently long (~ 100 nm), G decreases with increasing ϵ_m . In contrast, if the nanopore is sufficiently short, G increases with increasing ϵ_m . If L_n is of medium



long, G is insensitive to the variation of ε_m .

To further investigate the influence of ε_m on G , we plot the axial variation in the cross-sectional averaged concentration in Figure 2-3. In the present case (pH 4), the nanopore surface is negatively charged so that K^+ accumulate inside the nanopore. As seen in Figure 2-3(a), for both values of ε_m the application of $V=-1V$ drives K^+ from the upper end of the nanopore to its lower end. This is because the electrostatic field coming from the charged nanopore surface is interfered by the relatively strong applied electric field [40]. In addition, the larger the ε_m the more the amount of K^+ accumulates near the lower end of nanopore, and specifically near the upper outer surface of the nanopore, which would be discussed later. In contrast, Figure 2-3(d) shows a symmetric concentration profile without any spike and an insignificant difference between the two cases of ε_m . As for Figure 2-3(b)(c), the concentration profiles of $\varepsilon_m = 0$ states the intrinsic electrostatic field in the nanopore is strong against the applied electric field except for the upper entrance, where the local depletion occurs; while $\varepsilon_m = 80$, the concentration profiles are qualitatively similar, but the enrichment at the lower entrance in Figure 2-3(b) is more remarkable than that in Figure 2-3(c), and thus reflects on the conductance.

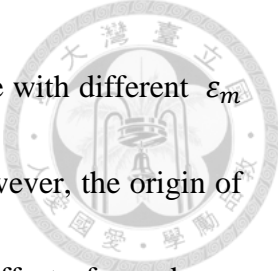
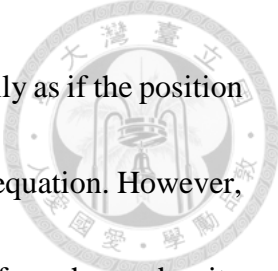
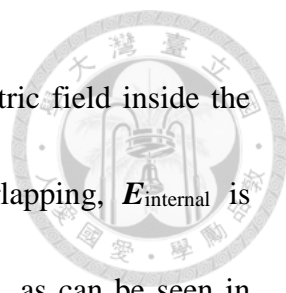


Figure 2-3 provides the explanations for the variation of conductance with different ε_m because the ionic flux is proportion to the accumulation of ions. However, the origin of the conductance enhancement is still attributed to the polarization effect of membrane occurred at the liquid/membrane surface as introduced previously. To distinguish the polarization effect on the conductance or ionic concentration profile, specifically in the case with shorten nanopore length, we plot the whole electrical potential profiles near the nanopore in Figure 2-4. Note that $\varepsilon_m=0$ implies the polarization effect of the membrane is not considered, thus the membrane domain Ω_m doesn't exist. While $\varepsilon_m=0.1$, the concentration profile and the electric potential profile in the fluid domain Ω_f are almost identical to the case $\varepsilon_m=0$, and so as the conductance, which implies the results are numerically converged as ε_m is closely to 0. The cases from $\varepsilon_m=0.1$ to $\varepsilon_m=80$ present that the electric potentials φ in Ω_f and Ψ in Ω_m are continuous ($\varphi=\Psi$) at the membrane surface to satisfy the continuum equation, however, we can observe the potential gradient $\nabla\varphi$ in Ω_f in the axial direction are remarkably different from $\nabla\Psi$ in Ω_m . The electric potential in Ω_m far from the nanopore surface varies uniformly in each case, while the profile varies upon ε_m in Ω_f . When ε_m is low, $\nabla\varphi$ in Ω_f is more intense at the upper-end of the nanopore; as ε_m raises, the electric potential varies more linearly, and Figure 2-S3(a) presents clearly with cross-sectional averaged electrical potential profile. The



linear change in the membrane domain can be also predicted analytically as if the position is far away from the nanopore surface because the eq (4) is a Laplace equation. However, the electrical potential near the nanopore surface is affected by the surface charge density and the radial electric field, thus it is more complicated to describe the profile. Based on the characteristic of the polarization, the induced dipole would suppress the local electric field. As the permittivity of membrane raises up, the radial electric fields in both fluid and membrane domains present less different, and then reflect on the electric potential gradient $\nabla\varphi$; for example, as $\varepsilon_m = \varepsilon_f = 80$, Figure 2-4(f) depicts the similar potential gradient in the both domains.

To summarize the influence of membrane polarization on the nanopore conductance, let us examine Figure 2-3, 2-4, and 2-S3 simultaneously for a comprehensive explanation. In the present case, cations are driven by $\nabla\varphi$ from the upper end of the nanopore towards its lower end. For the case of $L_n = 20$ nm if ε_m is small, $\nabla\varphi$ decreases rapidly from the nanopore upper end, so is the driving force for ionic transport. Therefore, cations accumulate near the nanopore lower end to satisfy the force balance. In contrast, if ε_m is large, because φ is influenced by the electric dipole field induced by the membrane ($\mathbf{E}_{\text{induced}}$) so that the decrease in the strength of $\nabla\varphi$ is slower than that when ε_m is small. Therefore, it is easier for cations to be driven out from the nanopore lower end, thereby

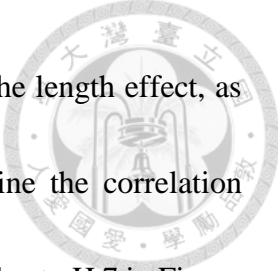


raising the conductance. At $L_n=1000$ nm, because the internal electric field inside the nanopore (E_{internal}) is influenced significantly by the EDL overlapping, E_{internal} is unaffected by neither the applied electric field (E_{applied}) nor E_{induced} , as can be seen in Figure 2-S3(d), so that G is almost independent of ϵ_m . If $L_n=100$ nm, the intrinsic electric field ($E_{\text{intrinsic}}$) in the nanopore is stronger than E_{applied} , which is opposite to the case of $L_n=20$ nm. In addition, as discussed previously, the induced dipole tends to suppress the local electric field so that the overlapping of EDL associated with $E_{\text{intrinsic}}$ is destroyed when ϵ_m is high. We conclude that the influence of the membrane permittivity on the nanopore conductance depends upon whether E_{internal} is dominated by $E_{\text{intrinsic}}$ or E_{applied} . In our case, if $L_n < 50$ nm, it is dominated by E_{applied} , and by $E_{\text{intrinsic}}$ if $L_n > 50$ nm.

2-3-2. Influence of the solution properties

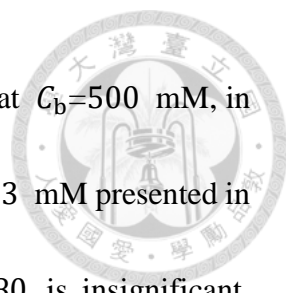
In the previous section, we found that the conductance is sensitive to the permittivity of membrane as the length of the nanopore is extremely short. Based on the above results, we further discuss the effects from the environment at such a short nanopore, $L_n=20$ nm.

As shown in Figure 2-5(a), the difference between the two permittivity is monotonically decreasing as the pH rising. While the pH deviates from pK_A of the carboxyl groups ($\sim\text{COOH}$), the surface of nanopore tends to accumulate more negative



charge and thus gain a strong intrinsic electric field. It is similar to the length effect, as the length is long enough, the difference would vanish. To examine the correlation between the pH and the length effects, we plot the concentration profile at pH 7 in Figure 2-5(b), and compare it with Figure 2-3(d). Except for the entrance effect occurring in Figure 2-5(b), the concentration profile is qualitatively similar, both presenting the plateau distribution, and therefore the similar results. This is because the plateau type concentration profile in **Fig. 3(d)** arises from that the strength of the intrinsic electric field established by the charged nanopore surface is stronger than that of the applied electric field. Similarly, the more the pH deviates from pK_A the higher the surface charge density, yielding a stronger intrinsic electric field and, therefore, a plateau type concentration profile

Figure 2-6(a) shows the variation of nanopore conductance G with the electrolyte concentration C_b under two different ϵ_m . When C_b raises, the two curves converge gradually, which implies the polarized dipole is crucial only at low C_b region. To explain the results, as predicted by several studies [10, 29, 41], G depends on C_b linearly at high C_b region because the bulk conductivity is much higher than the surface conductivity; as a result, no matter how the induced dipole varies the properties of the surface charge, the dominant term for G is still governed by the bulk conductivity. As shown in Figure 2-



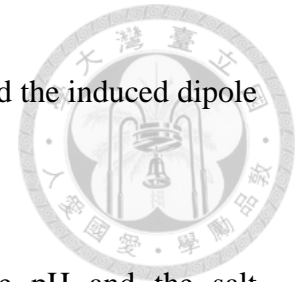
6(b), the concentration magnitude of K^+ and Cl^- are nearly the same at $C_b=500$ mM, in other words, the ICP effect in the nanopore is weak compared to $C_b=3$ mM presented in Figure 2-3, in addition, the difference between $\epsilon_m=0$ and $\epsilon_m=80$ is insignificant, which supports the argument that G is dominated by bulk conductivity at high C_b . At low C_b region, G is dominated by surface conductivity; in addition, as discussed previously, the induced dipole amplifies the internal electric field, therefore the curve of $\epsilon_m=80$ deviated linearly much more than $\epsilon_m=0$.

2-4. Conclusions

The manuscript presents the numerical results aimed at understanding the ionic transport behaviors in a cylindrical nanopore with the consideration of the membrane permittivity. The theoretical model is based on the continuum dynamics, composed of PNP and NS equations.

We found that in nanopores with a short length below 50 nm, the presence of the membrane permittivity led to a significant enhancement of the ionic conductance; on the contrary, we also found that the length in the middle scale, a slight suppression occurs, however, as the length prolongs above 500 nm, the conductance shows an independence of the membrane permittivity. The results stem from the competition between the intrinsic

electric field of the charged surface and the applied electric field, and the induced dipole plays a role to suppress the stronger one.

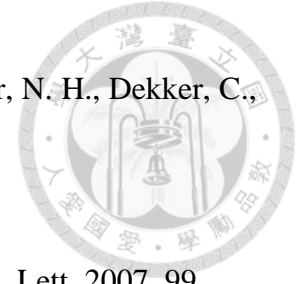


In addition, we also examine the effects of the electrolyte pH and the salt concentration, and the results show that the conductance enhancement by the dielectric membrane would be amplified at a lower value of both parameters. First, as pH is high enough, which means surface is highly negatively charged, in comparison, the induced dipole is relatively weak, thus the presence of the induced dipole becomes insignificantly. By understanding the composition of ionic conductance, including bulk conductivity and surface conductivity, the effect of the induced dipole diminishes as the bulk concentration is high enough to neglect the surface conductivity.

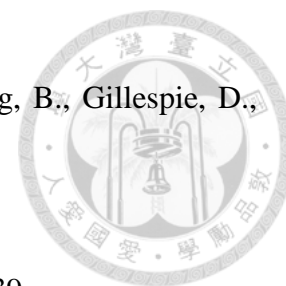
References



- [1] Zhou, M., Zhai, Y. M., Dong, S. J., *Anal. Chem.* 2009, 81, 5603-5613.
- [2] Pumera, M., Ambrosi, A., Bonanni, A., Chng, E. L. K., Poh, H. L., *Trac-Trends in Anal. Chem.* 2010, 29, 954-965.
- [3] Yadav, V., Roy, S., Singh, P., Khan, Z., Jaiswal, A., *Small* 2019, 15.
- [4] Karnik, R., Fan, R., Yue, M., Li, D. Y., Yang, P. D., Majumdar, A., *Nano Lett.* 2005, 5, 943-948.
- [5] Hsu, W. L., Inglis, D. W., Jeong, H., Dunstan, D. E., Davidson, M. R., Goldys, E. M., Harvie, D. J. E., *Langmuir* 2014, 30, 5337-5348.
- [6] Yang, C., Hinkle, P., Menestrina, J., Vlassioux, I. V., Siwy, Z. S., *J. Phys. Chem. Lett.* 2016, 7, 4152-4158.
- [7] Arico, A. S., Bruce, P., Scrosati, B., Tarascon, J. M., Van Schalkwijk, W., *Nat. Mater.* 2005, 4, 366-377.
- [8] Rolison, D. R., Long, J. W., Lytle, J. C., Fischer, A. E., Rhodes, C. P., McEvoy, T. M., Bourga, M. E., Lubers, A. M., *Chem. Soc. Rev.* 2009, 38, 226-252.
- [9] Chabot, V., Higgins, D., Yu, A. P., Xiao, X. C., Chen, Z. W., Zhang, J. J., *Energy Environ. Sci.* 2014, 7, 1564-1596.



- [10] Smeets, R. M. M., Keyser, U. F., Krapf, D., Wu, M. Y., Dekker, N. H., Dekker, C., Nano Lett. 2006, 6, 89-95.
- [11] Kim, S. J., Wang, Y. C., Lee, J. H., Jang, H., Han, J., Phys. Rev. Lett. 2007, 99.
- [12] Zangle, T. A., Mani, A., Santiago, J. G., Chem. Soc. Rev. 2010, 39, 1014-1035.
- [13] Vlassiouk, I., Smirnov, S., Siwy, Z., Nano Lett. 2008, 8, 1978-1985.
- [14] Cao, L. X., Wen, Q., Feng, Y. P., Ji, D. Y., Li, H., Li, N., Jiang, L., Guo, W., Adv. Funct. Mater. 2018, 28.
- [15] Cervera, J., Schiedt, B., Neumann, R., Mafe, S., Ramirez, P., J. Chem. Phys. 2006, 124.
- [16] Constantin, D., Siwy, Z. S., Phys. Rev. E 2007, 76.
- [17] Wang, X. W., Xue, J. M., Wang, L., Guo, W., Zhang, W. M., Wang, Y. G., Liu, Q., Ji, H., Ouyang, Q. Y., J. Phys. D-Applied Phys. 2007, 40, 7077-7084.
- [18] Schoch, R. B., Han, J. Y., Renaud, P., Rev. Mod. Phys. 2008, 80, 839-883.
- [19] Yeh, L. H., Zhang, M. K., Qian, S. Z., Anal. Chem. 2013, 85, 7527-7534.
- [20] Lin, C. Y., Yeh, L. H., Siwy, Z. S., J. Phys. Chem. Lett. 2018, 9, 393-398.
- [21] Bandini, S., Vezzani, D., Chem. Eng. Sci. 2003, 58, 3303-3326.
- [22] Boda, D., Valisko, M., Eisenberg, B., Nonner, W., Henderson, D., Gillespie, D., J. Chem. Phys. 2006, 125.



- [23] Boda, D., Nonner, W., Valisko, M., Henderson, D., Eisenberg, B., Gillespie, D.,
Biophys. J. 2007, 93, 1960-1980.
- [24] Boda, D., Henderson, D., Gillespie, D., J. Chem. Phys. 2013, 139.
- [25] Antila, H. S., Luijten, E., Phys. Rev. Lett. 2018, 120.
- [26] Wu, H. X., Li, H. H., Solis, F. J., de la Cruz, M. O., Luijten, E., J. Chem. Phys. 2018,
149.
- [27] Yuan, J. X., Antila, H. S., Luijten, E., Acs Macro Letters 2019, 8, 183-187.
- [28] Buyukdagli, S., Manghi, M., Palmeri, J., J. Chem. Phys. 2011, 134.
- [29] Lee, C., Joly, L., Siria, A., Biance, A. L., Fulcrand, R., Bocquet, L., Nano Lett. 2012,
12, 4037-4044.
- [30] Zhang, B. K., Ai, Y., Liu, J., Joo, S. W., Qian, S. Z., J. Phys. Chem. C 2011, 115,
24951-24959.
- [31] Siwy, Z., Gu, Y., Spohr, H. A., Baur, D., Wolf-Reber, A., Spohr, R., Apel, P.,
Korchev, Y. E., Europhys. Lett. 2002, 60, 349-355.
- [32] Siwy, Z., Heins, E., Harrell, C. C., Kohli, P., Martin, C. R., J. Am. Chem. Soc. 2004,
126, 10850-10851.
- [33] Zhang, H. C., Hou, X., Hou, J., Zeng, L., Tian, Y., Li, L., Jiang, L., Adv. Funct.
Mater. 2015, 25, 1102-1110.

[34] Zeng, Z. P., Ai, Y., Qian, S. Z., Phys. Chem. Chem. Phys 2014, 16, 2465-2474.

[35] Lund, M., Jonsson, B., Woodward, C. E., J. Chem. Phys. 2007, 126.

[36] Tagliazucchi, M., Rabin, Y., Szleifer, I., ACS Nano 2013, 7, 9085-9097.

[37] Eckstein, Y., Yossifon, G., Seifert, A., Miloh, T., J. Colloid Interface Sci. 2009, 338, 243-249.

[38] Hall, J. E., J. Gen. Physiol. 1975, 66, 531-532.

[39] Kowalczyk, S. W., Grosberg, A. Y., Rabin, Y., Dekker, C., Nanotechnology 2011, 22.

[40] Yeh, L. H., Zhang, M., Qian, S., Hsu, J. P., Tseng, S., J. Phys. Chem. C 2012, 116, 8672-8677.

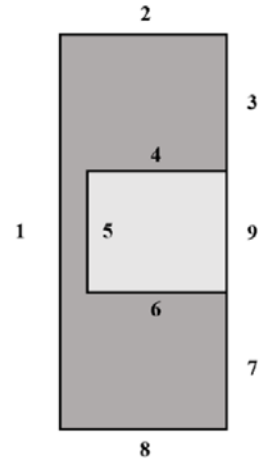
[41] Balme, S., Picaud, F., Manghi, M., Palmeri, J., Bechelany, M., Cabello-Aguilar, S., Abou-Chaaya, A., Miele, P., Balanzat, E., Janot, J. M., Scientific Reports 2015, 5.





Table 2-1. Boundary conditions assumed for eq (1)-(6)

surface	Poisson	Nernst–Planck	Navier–Stokes
1	Axial symmetry		
2	$\varphi = 0$	$c_i = c_{i0}$	$p = 0$
8	$\varphi = V_0$		
3, 7	$-\mathbf{n} \cdot \nabla\varphi = 0$	$\mathbf{n} \cdot \mathbf{N}_i = 0$	slip
4, 5, 6	$\mathbf{n} \cdot (-\varepsilon_0 \varepsilon_f \nabla\varphi)$ $+ \mathbf{n} \cdot (-\varepsilon_0 \varepsilon_m \nabla\Psi)$ $= \sigma$		$\mathbf{u} = \mathbf{0}$
9	$-\mathbf{n} \cdot \nabla\varphi = 0$	None	None



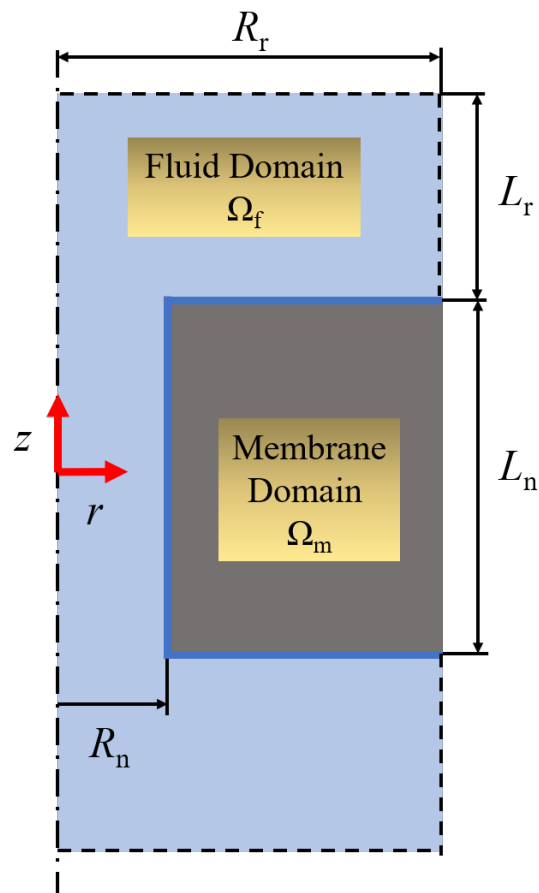


Figure 2-1. A charged cylindrical nanochannel of radius R_n and axial length L_n prepared from a dielectric membrane. The nanochannel connects two large, identical reservoirs filled with an aqueous salt solution. A computation domain Ω comprising the nanochannel and a cylindrical domain of length L_r and R_r in each reservoir is defined. The upper reservoir is grounded, and a potential bias V_0 is applied to the lower one. The cylindrical coordinates (r, z) are adopted with the origin at the nanochannel center.

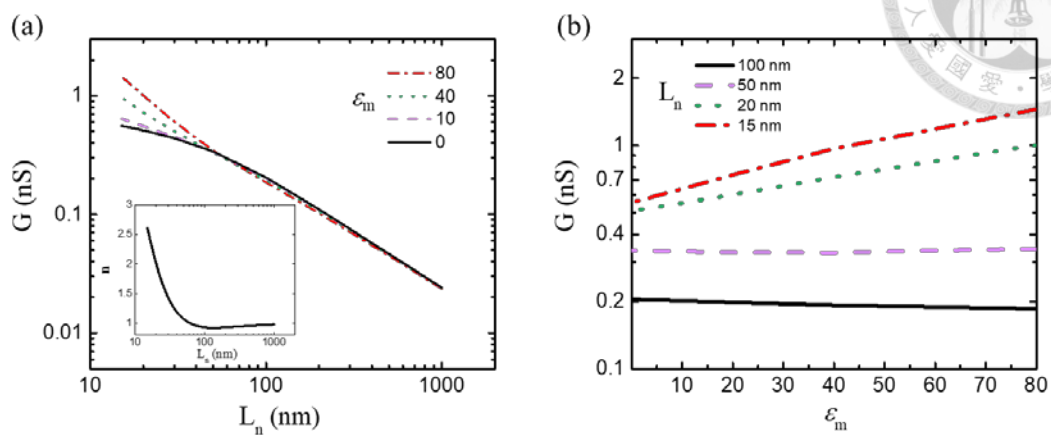


Figure 2-2. (a) Variation of nanopore conductance G with its length L_n at various levels of ϵ_m , (a), and variation with ϵ_m at various levels of L_n , (b), at $C_b=3$ mM, $R_n=5$ nm, and pH 4. Insert in (a): variation of the conductance ratio $n = G(\epsilon_m=80)/G(\epsilon_m=0)$ against L_n .

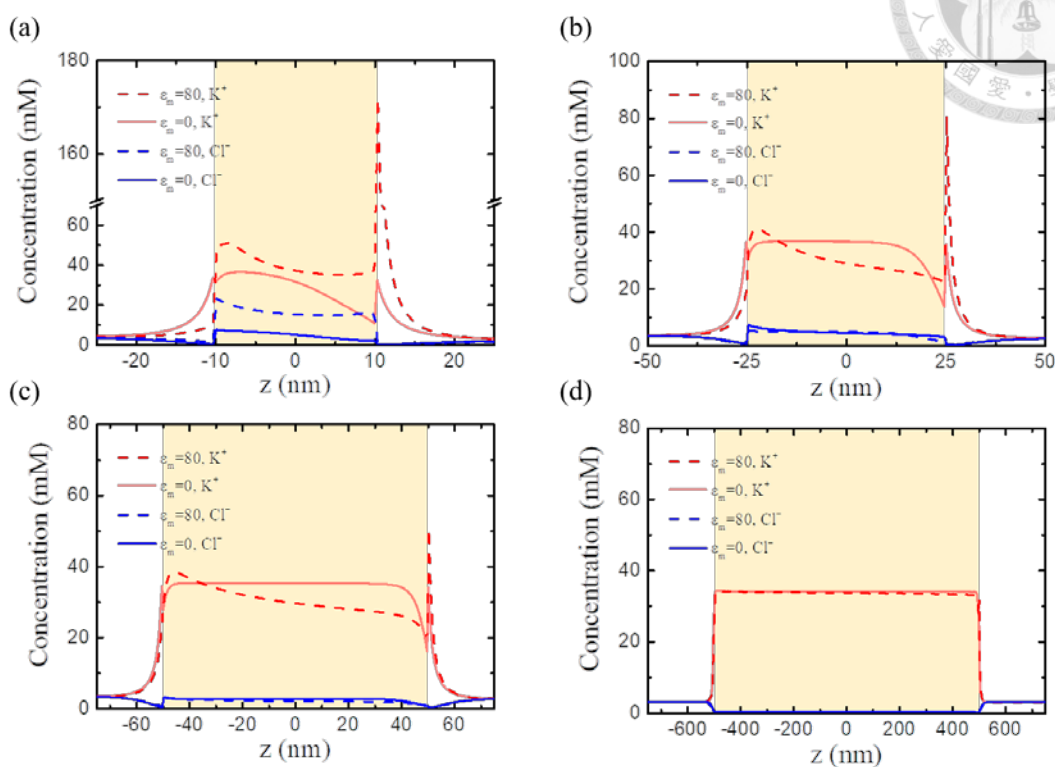


Figure 2-3. Cross-sectional averaged concentration profile of K^+ and Cl^- at pH 4 and $C_b=3$ mM, and the radius of nanopore $R_n=5$ nm. (a) $L_n=20$ nm, (b) $L_n=50$ nm, (c) $L_n=100$ nm, (d) $L_n=1000$ nm.

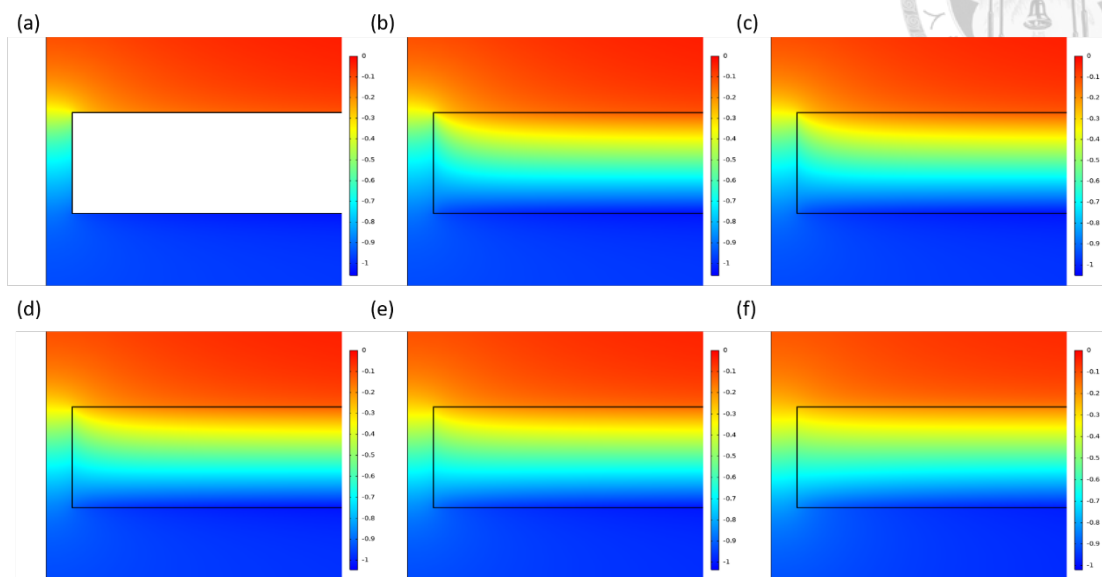


Figure 2-4. Profiles of the electric potential in the liquid phase and inside membrane for various levels of ϵ_m . (a) $\epsilon_m=0$, (b) $\epsilon_m=0.1$, (c) $\epsilon_m=10$, (d) $\epsilon_m=20$, (e) $\epsilon_m=40$, (f) $\epsilon_m=80$. The parameters used are the same as those in Figure 2-3(a).

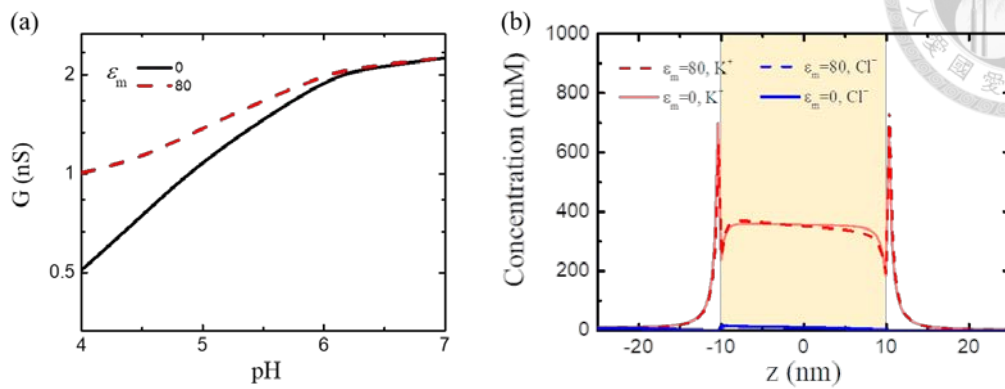


Figure 2-5. (a) Conductance of the nanopore versus the pH for $\epsilon_m=80$ and 0 at $C_b=3$ mM and the dimensions of nanopore $L_n=20$ nm, $R_n=5$ nm. (b) Cross-sectional averaged concentration profile of K^+ and Cl^- at pH 7.

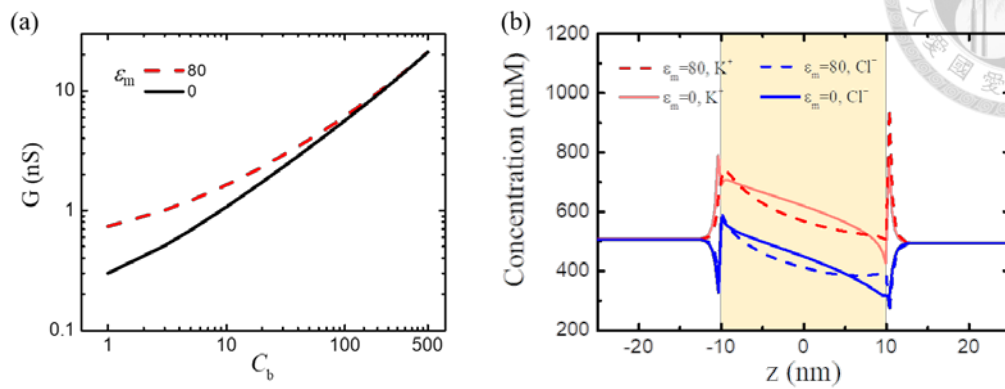


Figure 2-6. (a) Conductance of the nanopore versus C_b for $\epsilon_m=80$ and 0 at pH 4 and the dimensions of nanopore $L_n=20$ nm, $R_n=5$ nm. (b) Cross-sectional averaged concentration profile of K^+ and Cl^- at $C_b=500$ mM.

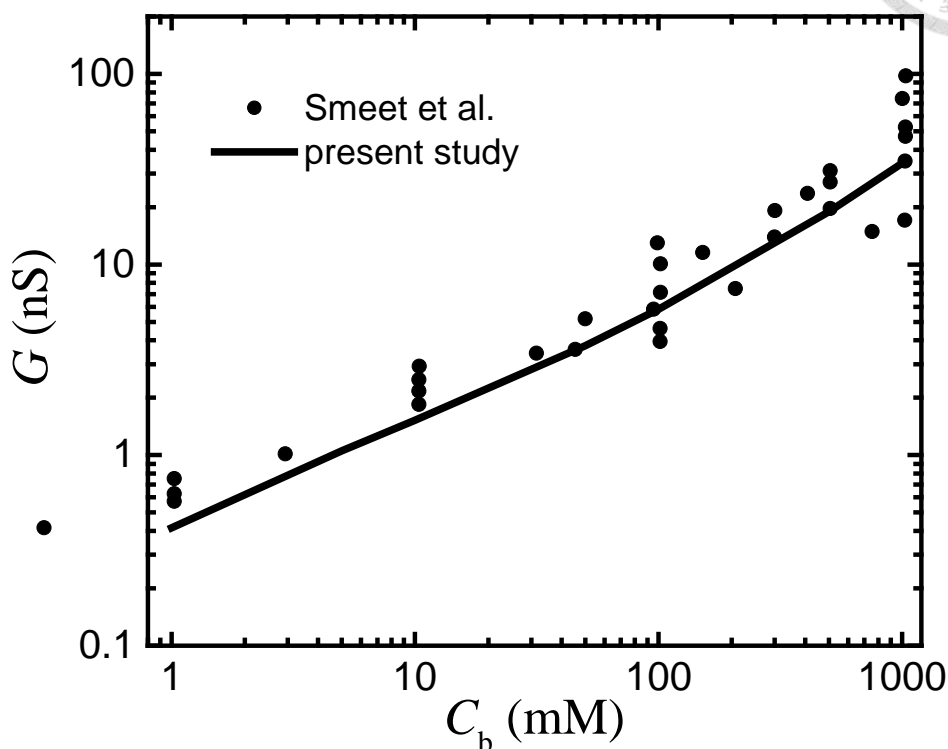


Figure 2-S1. Conductance in a pH-regulated silica nanopore of length $L_n=34$ nm as a function of C_b at pH 7.5: symbols are selected from the experimental data of Smeets et al.; solid lines present the numerical results at $R_n=5.1$ nm, $pK_A=7$, $pK_b=1.9$, $\Gamma_t=4.8$ nm⁻² and $\varepsilon_m=3.8$.

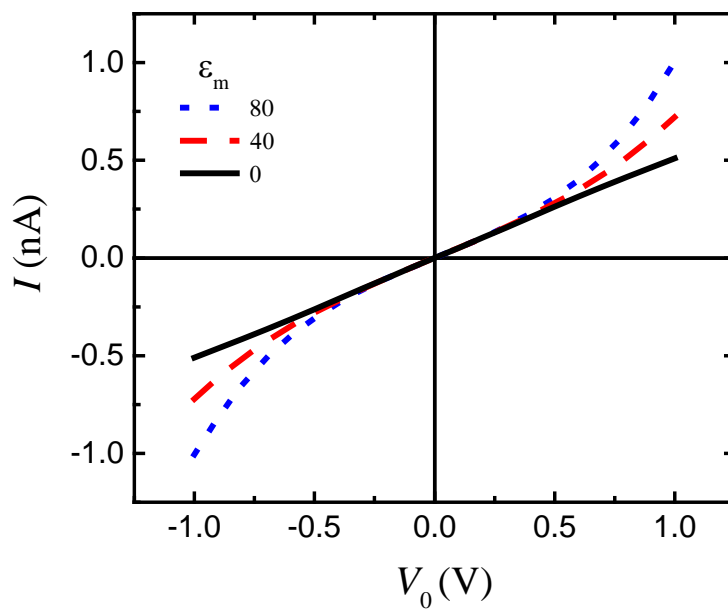


Figure 2-S2. Simulated current-voltage curves for various levels of ϵ_m at $R_n=5$ nm,

$L_n=20$ nm, $C_b=3$ mM, and pH 4.

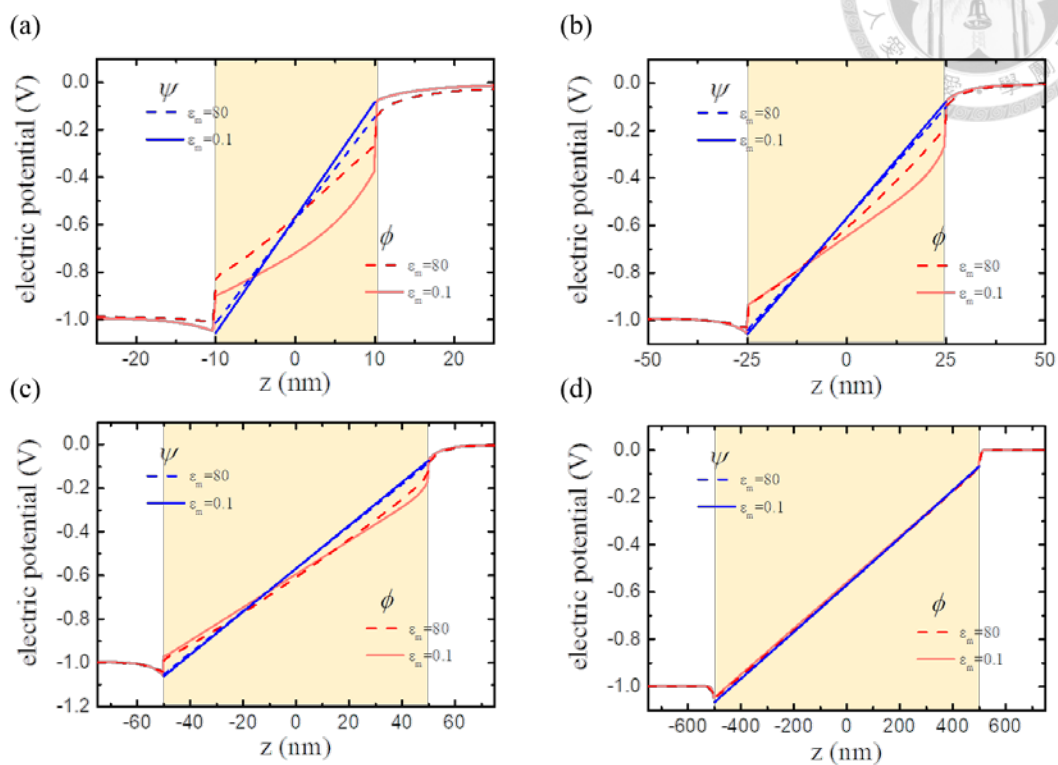


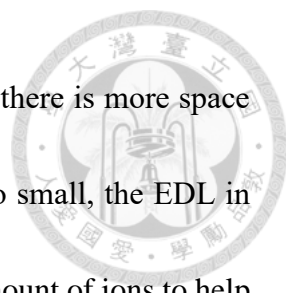
Figure 2-S3. Axial variations in the cross-sectional averaged electric potentials ϕ and Ψ for various values of L_n at $C_b=3$ mM, $R_n=5$ nm, and pH 4. (a) $L_n=20$ nm, (b) $L_n=50$ nm, (c) $L_n=100$ nm, (d) $L_n=1000$ nm.



Conclusion




In chapter 1, we focus on the ionic current rectification (ICR) behavior of nanochannels having nonuniform cross-section. We show that a large ratio γ (=radius of larger channel/radius of smaller channel) yields a greater current at a negatively applied voltage bias, but not necessary at a positively applied voltage bias. As γ increases the nanochannel resistance decreases monotonically but the concentration of ions in the nanochannel shows a local maximum, and the latter effect dominates the current. If a positive voltage bias is applied, the enrichment of ions in the nanochannel makes the interaction of ions and nanochannel surface important. In this case, the geometry of the nanochannel is important because it influences directly on the profile of ions inside. In contrast, if a negative voltage bias is applied, the depletion of ions in the nanochannel makes the profile of ions, and therefore, their interaction with the nanochannel surface insensitive to the nanochannel geometry. Therefore, the ICR factor R_f exhibits a local maximum as γ varies. R_f also exhibits a local maximum as the ratio λ (=length of smaller channel/total channel length) varies. This local maximum occurs at a small value of λ (i.e., the smaller segment of the nanochannel is short). If λ is large, ions accumulate appreciably in the smaller segment of the nanochannel making the difference between the current at a positively applied voltage bias and that at a negatively applied voltage biases



insignificant so that ICR is not significant. As λ gets small, because there is more space for ion enrichment/depletion, R_f becomes large. However, if λ is too small, the EDL in the smaller segment of a nanochannel is unable to confine enough amount of ions to help accumulating ions in its larger segment so that ICR is insignificant. The variation of the solution pH also leads to a local maximum in R_f . This can be explained by the variations in the conductivity and the current at different applied voltage biases. The current in the preferential direction is nearly proportional to the extent of the deviation of pH from IEP, but it is not the case in the opposite direction of the current. In the latter, the current increases first with the degree of deviation of pH from IEP, but becomes insensitive to that deviation if pH is sufficiently far from IEP. The results gathered in our study provide desirable and necessary information for both the design of relevant devices and the optimization of their performance.

In chapter 2, we present the results of the ionic transport behavior in a cylindrical nanopore with the consideration of the membrane permittivity. We found that in nanopores with a short length below 50 nm, the presence of the membrane permittivity led to a significant enhancement of the ionic conductance; on the contrary, we also found that the length in the middle scale, a slight suppression occurs, however, as the length prolongs above 500 nm, the conductance shows an independence of the membrane



permittivity. The results stem from the competition between the intrinsic electric field of the charged surface and the applied electric field, and the induced dipole plays a role to suppress the stronger one. In addition, we also examine the effects of the electrolyte pH and the salt concentration, and the results show that the conductance enhancement by the dielectric membrane would be amplified at a lower value of both parameters. First, as pH is high enough, which means surface is highly negatively charged, in comparison, the induced dipole is relatively weak, thus the presence of the induced dipole becomes insignificantly. By understanding the composition of ionic conductance, including bulk conductivity and surface conductivity, the effect of the induced dipole diminishes as the bulk concentration is high enough to neglect the surface conductivity.